High-temperature oxidation of AlCrFeNi-(Mn or Co) high-entropy alloys: effect of atmosphere and reactive element addition

Chongchong Tang [a], Hao Shi [b], Adrian Jianu [b], Alfons Weisenburger [b], Geanta Victor [c], Mirco Grosse [a], Georg Müller [b], Hans Jürgen Seifert [a], Martin Steinbrück [a]

[a] Institute for Applied Materials (IAM), Karlsruhe Institute of Technology (KIT), Hermann-von-Helmholtz-Platz 1, 76344 Eggenstein-Leopoldshafen, Germany

[b] Institute for Pulsed Power and Microwave Technology, Karlsruhe Institute of Technology (KIT), Hermann-von-Helmholtz-Platz 1, 76344 Eggenstein-Leopoldshafen, Germany

[c] Materials Science and Engineering Faculty, University POLITEHNICA of Bucharest, Splaiul Independentei 313, 060042, Bucharest, Romania

Corresponding author: Chongchong Tang, Chongchong.tang@kit.edu

Abstract:

The effects of atmosphere (oxygen and steam) and reactive element addition (Zr and Y) on high-temperature oxidation behavior of $Al_{0.5}$CrFeNiMn and $Al_{0.5}$CrFeNiCo high-entropy alloys at 1000°C and 1200°C were studied. The $Al_{0.5}$CrFeNiMn alloy displayed different oxidation mechanisms in oxygen and steam owing to differing oxygen partial pressures and preferential oxidation of Mn. A protective alumina scale established on $Al_{0.5}$CrFeNiCo alloy in both atmospheres and the beneficial effects of Y addition are seen by remarkably improved oxide scale adherence and suppression of convoluted oxide scale morphology. However, doping with 1 wt.% Zr deteriorates the oxidation resistance with substantial Al+Zr internal oxidation.

Keywords: high entropy alloys (HEAs); high temperature oxidation; steam; reactive element; oxidation kinetics

1. Introduction

Improving the efficiency and sustainability of energy systems with progressively higher operating temperatures and pressures continuously demands advanced structural materials with exceptional mechanical strength and corrosion resistance at elevated temperatures [1–3]. Conventional alloy development strategies are normally based on one or two main components with minor alloying elements to achieve desirable properties [4]. The harmonious and simultaneous development of high-temperature mechanical properties and corrosion resistance are challenging for such conventional alloys. For instance, alumina-forming FeCrAl alloys possess excellent high-temperature oxidation resistance but display rapidly reduced strength with increasing temperatures [5]. A new class of alloys that conceivably overcome this compromise are high-entropy alloys (HEAs) [6–9]. From a chemical composition perspective, HEAs and the related concept of multi-principal element alloys or complex concentrated alloys are typically defined as alloys that are composed of five or more principal elements with molar ratios ranging from 5 % to 35 % [8]. Their high configurational entropy (maximum $R \cdot \ln N$; R is the gas constant and N is the number of components in the system) favors the formation of solid solution phases with reduced tendency to form intermetallic compound phases (with lower configurational entropy) [7]. HEAs often have exceptional or adjustable mechanical and physical properties, superior structural stability as well as good oxidation/corrosion resistance [7,8,10]. Their unique properties are proposed associated with four core effects, namely 1) high mixing entropy, 2) sluggish diffusion, 3) severe lattice distortion, and 4) cocktail effects. They thus have attracted numerous attentions for many structural and high-temperature applications in harsh environments, and also stimulate new ideas and directions on materials exploration [11,12].

Initial explorations of HEAs mainly focused on searching of single-phase solid solution alloys with principally either body center cubic (BCC) or face centered cubic (FCC) structures [13,14], and rare hexagonal close packed (hcp) structure [15]. Research findings demonstrated that their mechanical properties are largely determined by their phase constitutions. Single-phase BCC alloys generally possess high strength and inadequate plasticity, while FCC alloys display low strength but better plasticity [7]. More recent studies reveal that solid solution dual-phase high entropy alloys could overcome the strength–ductility trade-off with combinations of high strength and good ductility via controlling the phase ratios and precipitations [16–19]. Among the numerous HEA design concepts, the AlCoCrFeMnNi and its sub-systems have been intensively investigated and unveil many interesting characteristics [7,20–25]. Their phase constitutions and mechanical properties are largely dependent on the Al content. Increasing the Al mole fraction from $Al_0CoCrFeNi$ to $Al_3CoCrFeNi$ can successively alter their phase constitution from single FCC, duplex FCC + BCC to single BCC, accompanied by improved hardness/strength and reduced ductility [21,25]. Therefore, via manipulating their Al content at an intermediate and appropriate level, superior mechanical properties both at normal and elevated temperatures can be achieved.

One of the most common failure mechanisms of structural components used at high-temperature environments is degradation by oxidation/corrosion [3]. Recently, the high-temperature oxidation performances of various HEA designs have been drawing great attention

for evaluating their application capacity in high-temperature corrosive environments [26–31]. HEAs with Al and/or Cr principal elements offer the possibilities to withstand high temperature oxidation reaching 1200°C via formation of thermally grown protective Al_2O_3 or Cr_2O_3 based scale, for example the aforementioned AlNiCoCrFe system [27]. Butler and Weaver tested a series of arc-melted $Al_x(NiCoCrFe)_{100-x}$ HEAs, where x equals 8 – 30 at.%, at 1050°C in air [32]. They found that the oxidized HEAs form an external Cr_2O_3 scale with Al_2O_3 subscale beneath. Increasing the Al content enhances the oxidation resistance of the HEAs. Similar observations were reported in other studies [26,28,33]. In addition, alike to other alumina-forming alloys (e.g. FeCrAl or NiCoCrAl), doping with reactive elements (RE, like Y, Zr, Hf, etc.) can bring beneficial REs effects with improved oxidation performance [27,33]. For instance, recently Lu et al. reported that Y-doped $AlCoCrFeNi_{2.1}$ eutectic high-entropy alloy revealed remarkably improved scale adhesion and suppressed formation of interfacial pores and scale wrinkling during oxidation at 1100°C in ambient air [34]. However, previous studies on understanding the oxidation behaviors of these HEAs were mainly performed in air or dry atmosphere with relatively low temperatures below 1200°C. Many industrial processes involve moisture-containing or pure steam atmospheres (such as inside turbines or power stations) and the influence of steam on the oxidation behavior of these alloys are rarely explored. In addition, the operating temperatures of many industrial systems can also rise remarkably under some extreme conditions [35]. Comparative studies on revealing the potential different oxidation mechanisms, oxidation kinetics and degradation behaviors in both dry and wet atmospheres, with/without RE-addition of these newly-developed HEAs up to significantly higher temperatures (such as 1200°C) are still lacking.

In this study, we systematically investigated the effects of oxidizing atmospheres (oxygen & steam), doping elements (Zr & Y), and alloying elements (Mn & Co) on oxidation mechanisms and kinetics of $Al_{0.5}$CrFeNi-based HEAs at 1000 and 1200°C. This work therefore focuses on the high-temperature oxidation behavior of four $Al_{0.5}$CrFeNi-(Mn or Co) based HEAs in two atmospheres: oxygen and steam. Two $Al_{0.5}$CrFeNiCo alloys were doped with low contents of zirconium and yttrium individually to elucidate the potential beneficial REs in both atmospheres. Transient oxidation tests up to 1300°C were first carried out to provide an overview on their oxidation performance. Isothermal oxidation tests were then performed at 1000°C and 1200°C in both oxygen and steam atmospheres for 20 hours. The oxidation mechanisms and kinetics were systematically and comparatively studied by means of thermogravimetric analysis (TGA) and oxide scale characterizations combined with thermodynamic modeling. The outcome of this study provides important insights on understanding the influence of oxidizing atmospheres and reactive elements on the oxidation behavior of HEAs, allowing for advanced alloy designs for widespread applications at high temperatures.

2. Experimental details

All four HEAs were prepared from high-purity alloying elements (purity>99.99%) by vacuum arc melting in an argon atmosphere. The prepared alloy ingots were flipped over and re-melted about five times to ensure a uniform mixture of all alloying elements. The alloying ingots were cut into cylindrical samples with dimensions of ~ 9 mm diameter and ~ 2 mm thickness, respectively. The two base sides were mechanically ground using 2500 grit SiC paper. Before test, they were cleaned with distilled water, isopropanol and acetone in an ultrasonic bath. Table 1 shows the chemical compositions of the four HEAs measured by energy dispersive X-ray spectroscopy (EDS). The molar concentration of aluminum is approximately half of the other four principal alloying elements. In HEA06, Mn was replaced by Co. HEA07 and HEA08 have similar chemical compositions to HEA06, except for doping with small amount of zirconium and yttrium, respectively.

Table 1 Chemical composition of the four high-entropy alloys

No.	*Mol.%*	*Wt.%*
HEA05	$Al_{11.1}Cr_{22.2}Fe_{22.2}Ni_{22.3}Mn_{22.2}$	$Al_{5.7}Cr_{22.1}Fe_{23.8}Ni_{25.0}Mn_{23.3}$
HEA06	$Al_{13.0}Cr_{21.7}Fe_{21.7}Ni_{21.8}Co_{21.7}$	$Al_{6.7}Cr_{21.5}Fe_{23.1}Ni_{24.3}Co_{24.3}$
HEA07	$Al_{12.7}Cr_{21.6}Fe_{21.7}Ni_{21.7}Co_{21.6}Zr_{0.06}$	$Al_{6.5}Cr_{21.3}Fe_{22.9}Ni_{24.1}Co_{24.1}Zr_{1.0}$
HEA08	$Al_{12.7}Cr_{21.6}Fe_{21.7}Ni_{21.7}Co_{21.6}Y_{0.06}$	$Al_{6.5}Cr_{21.3}Fe_{22.9}Ni_{24.1}Co_{24.1}Y_{1.0}$

Two different types of oxidation tests were performed, i.e. transient and isothermal. Oxidation experiments were carried out with two Netzsch simultaneous thermal analyzers (STA), one working in dry atmospheres (STA-409) and the other one allowing to produce steam with a steam generator and special water vapor furnace (STA-449). The transient tests were implemented from room temperature to 1300°C with a heating rate of 5 K/min and subsequent holding at 1300°C for 10 min in a flowing, pure oxygen atmosphere. These tests are designed to outline the oxidation resistances of the four HEAs and assist in selecting appropriate oxidation temperatures for the isothermal tests.

The isothermal tests were carried out at 1000°C and 1200°C for 20 hours in pure O_2 and H_2O atmospheres. In both systems, the samples were placed on an alumina sample holder in the furnace enclosure. They were heated to the pre-defined temperature (1000°C or 1200°C) with a heating rate of 20 K/min and maintained for 10 minutes to stabilize the temperature in an argon flow. Reactive gas (oxygen or steam) was then injected into the furnace, while the samples were isothermally exposed for 20 hours. The flow rate for oxygen and steam were 10 L/h and 3 g/h (steam produced via liquid water flow), respectively. The exhaust gas was collected and processed by the ventilation system inside the building to avoid accumulation in the lab. An argon flow circulates constantly between the enclosure and the balance to avoid the reactive gas flow into the balance. After 20 hours exposure, the reactive gases injection was switched off and the samples were quickly cooled in argon flow. Additionally, reference tests using an alumina slice with similar geometry instead of alloy sample were performed under same parameters. The mass change of the sample was *in-situ* recorded during the test allowing to determine their oxidation kinetics later.

The phase constitution and microstructure of the fresh alloys were characterized by X-ray diffraction (XRD, Seifert PAD II) and scanning electron microscopy (SEM, Philips XL30S). XRD patterns were recorded in Bragg–Brentano geometry (θ-2θ) with a step size of 0.02° and a scan speed of 1°/min with Cu Kα1 radiation (λ=0.15406 nm). Each sample was weighed before and after the oxidation test. The visual image of the samples after test were taken using a digital camera. XRD analyses were performed to determine the phases present in the sample surface after oxidation. Then, the samples were prepared to be observed with the SEM. They were first cleaned with acetone in an ultrasonic bath since particles on the sample after oxidation can cause contamination in SEM. It is necessary to point out that such cleaning removes some loosely adhered oxide particles on the sample surface. Samples were then covered with a thin gold layer to make them conductive. Surface observations and composition analyses of the samples were made with SEM equipped with an EDS detector. After the surface evaluation, the samples were electroplated with a nickel layer of approximately 40 μm thickness. At that moment they were embedded and polished by standard metallographic techniques, and further analyzed by SEM/EDS of cross-sectional composition and structure.

3. Results

3.1 Phase constitution and microstructure of fresh alloys

Fig. 1 shows the XRD patterns of the four HEAs before oxidation test. As expected, these alloys are composed of dual phase constitution, both BCC (disordered and ordered) and FCC phases. This observation is consistent with previous studies that for such AlNiCrFe(CoMn)-based alloys increasing the Al content to a moderate level promotes the dual phase composition [21,25,32,36]. The principal phase for HEA05 is BCC, while for the other three Co-containing alloys is FCC. This dissimilarity is mainly because of Co being a well-known strong FCC former in HEAs [7] .

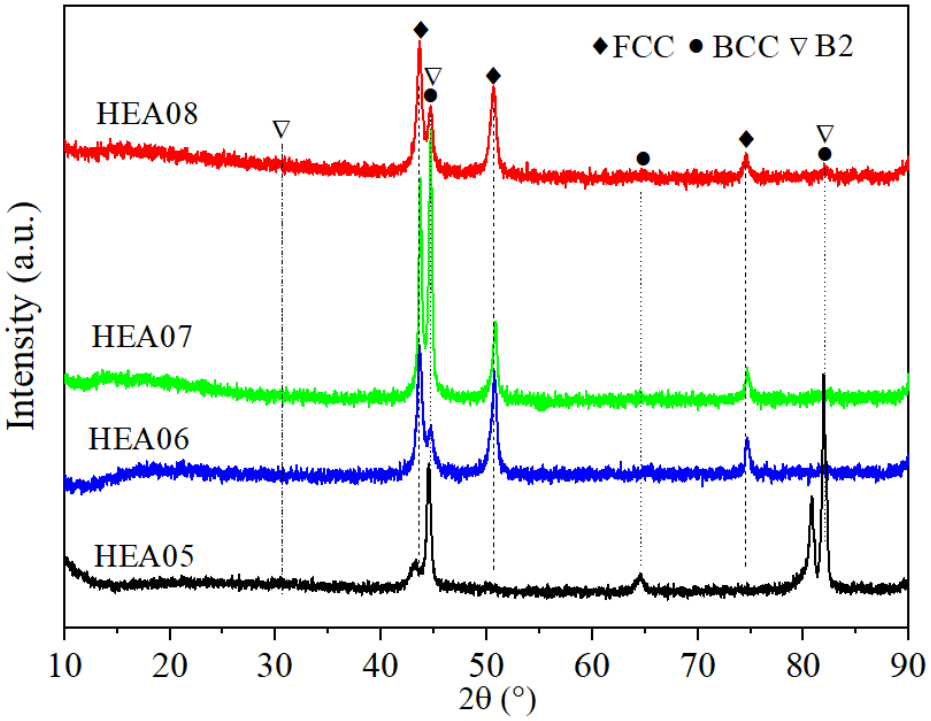

Fig. 1. XRD patterns of the four alloys before oxidation test.

The microstructures of the four as-cast HEAs before oxidation test are displayed in Fig. 2. All four alloys solidified dendritically with Cr, Fe, Mn or Co rich dendritic (D) regions and Ni, Al rich interdendritic (ID) regions. The D regions are composed of FCC phase as matrix. The ID regions consist of disordered solid solution BCC phase and B2-NiAl phase (ordered BCC) precipitates from spinodal decomposition [7]. The phase constitutions and microstructures herein are consistent with the chemically analogous HEAs reported previously [7,32,36].

In case of the HEA07 and HEA08, the reactive element additive (Zr and Y) essentially segregates at boundaries of the dendrites, limiting their grain growth/coalescence and resulting in a grain refinement effect, Fig. 2 (c) and (d). The chemical composition analysis revealed that these precipitates are enriched both in reactive element (Zr or Y) and Ni. The lower chemical mixing enthalpies between the reactive element and Ni compared to other alloying elements, as reported previously [37], plausibly induce their co-segregation. The segregation of such Zr or Y-containing

compound is commonly because of an over-doping that their concentrations exceed the solubility limit in the matrix [37].

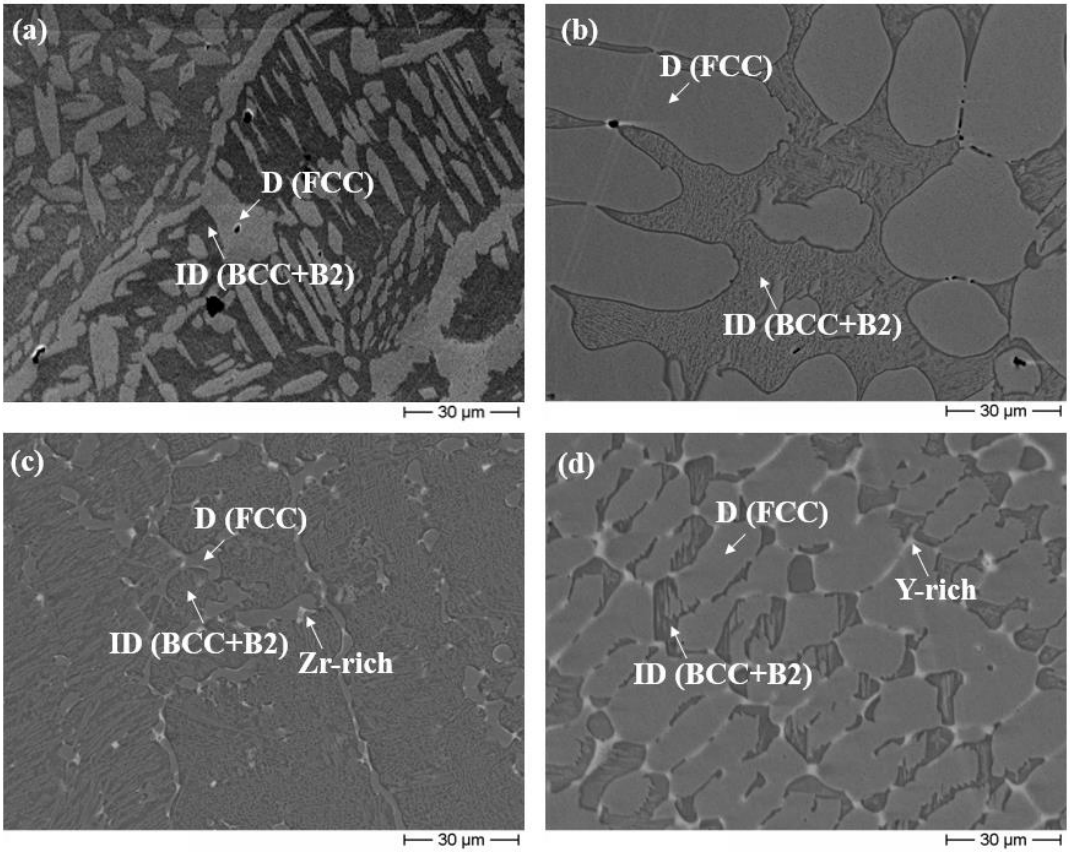

Fig. 2. Microstructure of the four HEAs before oxidation test, (a) HEA05, (b) HEA06, (c) HEA07, (d) HEA08.

3.2 High-temperature oxidation

3.2.1 Transient tests

Fig. 3 presents the temperature profile and mass change variations recorded during the transient tests in O_2 atmosphere. Evidently, the HEA05 exhibits the worst oxidation resistance among the four alloys. It exhibits the highest mass gain during the test, followed by HEA07 and HEA06/HEA08, respectively. Its mass curve rises gradually up to ~180 minutes, with the temperature reaching about 950°C. From 1000°C, after oxidation time beyond 200 minutes, the oxidation rate of HEA05 accelerated significantly and the mass started increasing rapidly up to 12 mg/cm² at the end of the test. This alloy underwent the strongest oxidation and the post-test appearance revealed substantial delamination of the external oxide scale.

The mass curves of the other three alloys, however, remained barely changed up to 1000°C. The mass of HEA07 then increases slightly until a mass gain of about 1.5 mg/cm². HEA06 and HEA08 show similar behaviors with very low mass gains of about 0.5 mg/cm² finally. The trivial mass gains are comparable to alumina-forming FeCrAl alloys under similar oxidation conditions [38], evidencing their excellent oxidation resistance with thermally grown alumina-based protective oxide scale (see next section).

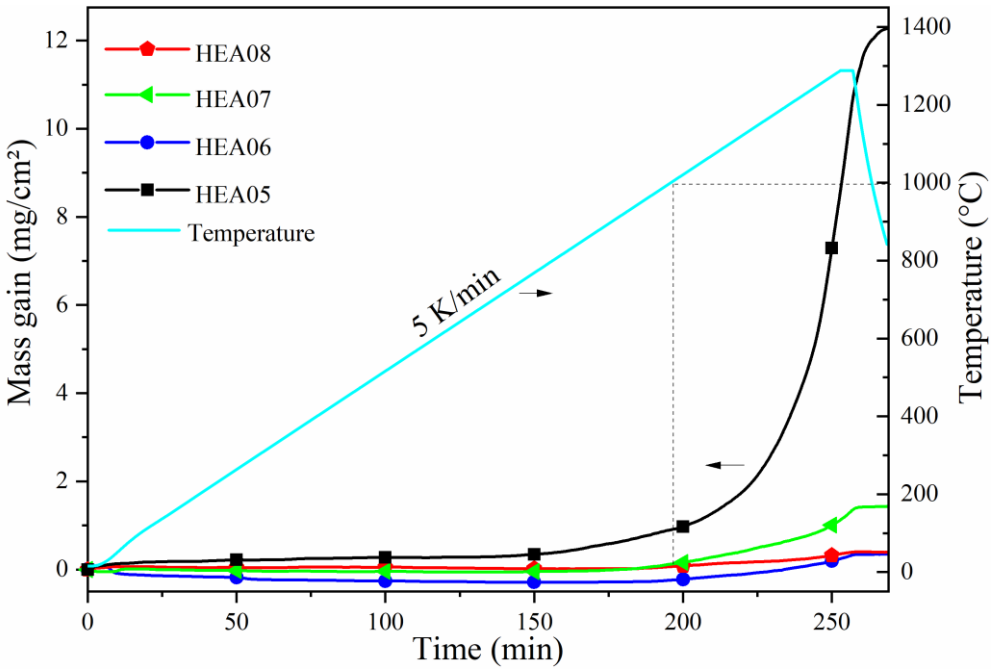

Fig. 3. Temperature profile and mass change of the four alloys during the transient tests to 1300°C in O2 atmosphere.

3.2.2 Isothermal tests in oxygen and steam at 1000°C and 1200°C

3.2.2.1 Surface appearances and oxidation kinetics

Fig. 4 are macro images showing the surface appearance of the samples after the isothermal oxidation. Except for HEA08, all other alloys exhibited visible, different levels of particles (oxide scale) spallation from the sample surface after oxidation. Oxidation at a higher temperature, 1200°C, resulted in obviously more pronounced peel off, owing to higher thermal stresses

generated by thermal expansion mismatch between the oxide scale and the alloy substrate during temperature change (cooling stage). The spallation levels of the oxide scale after oxidation at 1200°C have been estimated by comparing the mass gain data recorded by STA and measured by analytical balance. The thermally grown oxide scale on HEA05 displays the strongest level of peel off both in steam (~98%) and in oxygen (~70%), followed by HEA07 and HEA06. All alloys showed higher levels of oxide scale peel off, 10~30% higher, after oxidation in steam than in oxygen. The oxide scales grown on HEA06 and HEA07 demonstrated comparatively convoluted and loose structure. On the other hand, the oxide layers on HEA08 displayed compact and smooth features without macroscopic representation of exfoliation for all four oxidized samples.

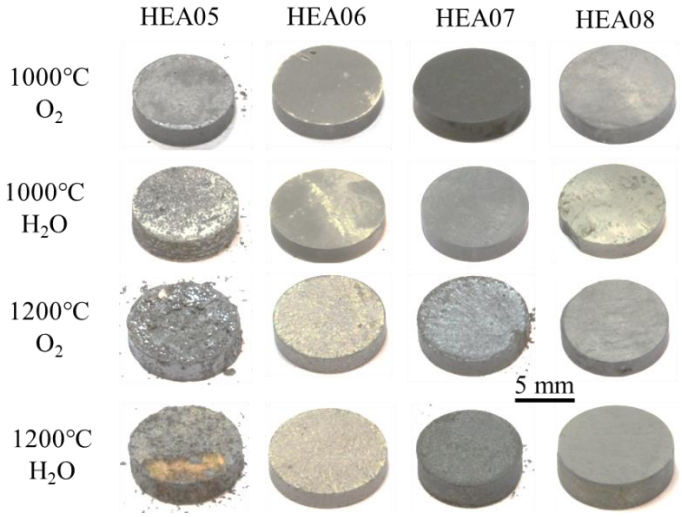

Fig. 4. Surface appearances of the alloys after the isothermal oxidation test for 20 h.

Fig. *5* shows the mass change results of the alloys during the isothermal oxidation at 1000°C and 1200°C in oxygen and steam for 20 h. All mass change curves here were plotted by subtracting the reference test made with an alumina slice. After subtraction of the reference, the mass changes of HEA06 and HEA08 at 1000°C became negative in a certain interval. This is likely due to the extremely low mass change of the samples approaching the accuracy limit (± 0.1 mg) of balance, small fluctuations in environment temperature and pressure during measurement, and different geometry/mass of the reference sample. In addition, the formation of volatile oxides and hydroxides, and peeling off of surface particles during oxidation exposure may also result in mass loss of the samples. Indeed, virtually no differences were seen by weighing the samples before and after the test.

Obviously different oxidation behaviors were seen for HEA05 (containing Mn) in oxygen and steam atmospheres. The mass gains are much higher in oxygen compared with those in steam at the same temperature. More specifically, the final mass gain in oxygen is ~ 4 times at 1000°C and ~ 6 times at 1200°C, respectively, higher than that in steam. In contrast, the other three alloys (containing Co) revealed similar oxidation properties in both oxygen and steam, featured by nearly overlapping mass change curves especially at 1200°C.

In addition, HEA05 displayed the fastest oxidation rate among the four alloys in both atmospheres, followed by HEA07. While at 1200°C, oxidation of HEA05 in steam yielded quite comparable mass gain tendency to HEA07. The final mass gain reached 37.1 mg/cm^2 for HEA05 in oxygen, and ~6.5 mg/cm^2 for HEA05 in steam and HEA07 in both oxygen and steam at 1200°C. HEA06 and HEA08 showed the equally excellent oxidation resistance, and their mass gains are below 1.5 mg/cm^2 after oxidation at 1200°C for 20 h.

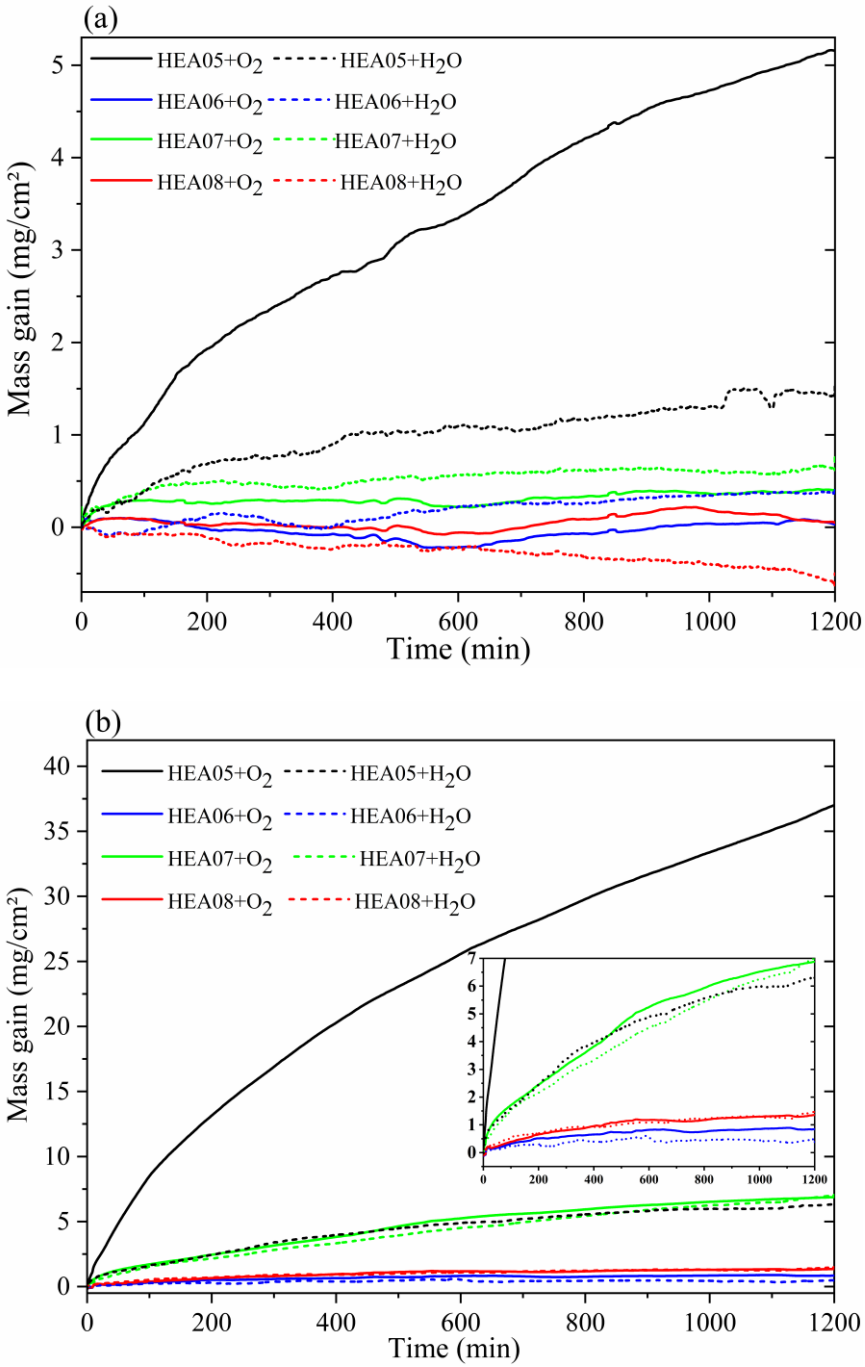

Fig. 5. Mass change curves of the alloys during isothermal oxidation test, (a) 1000°C and (b) 1200°C.

As seen in Fig. 5, the mass change curves imply that the isothermal oxidation kinetics of these four alloys generally obey the parabolic rate law. Thus, the relationship between the mass gain per unit surface area ($\Delta m/A$) and oxidation time (t) can be expressed as follows:

$$(\Delta m/A)^2 = k_p t$$

To quantitatively compare their oxidation performance, the parabolic oxidation rate coefficients k_p of the four alloys were calculated and the results are shown in Table 2. The coefficients for HEA06, HEA07 and HEA08 at 1000°C were not given because of their exceedingly low mass changes causing large uncertainties and errors in data interpretation. While for other conditions listed in Table 2 the coefficient of determination (R^2) are typically above 0.90, indicating excellent fitting outcomes with parabolic law.

The HEA05 shows the highest rate coefficients in oxygen among the four alloys at 1200°C, which is also more than one order of magnitude higher than that in steam. The rate coefficients for HEA05 in steam and HEA07 in both oxygen and steam are quite similar, one order of magnitude higher than those of HEA06 and HEA08. The rate coefficients of HEA08 are the second smallest with identical values in oxygen and steam at 1200°C. The HEA06 displayed the lowest rate coefficients, even slightly lower than those of HEA08. Moreover, the rate coefficients for HEA06 and HEA07 in steam is slightly smaller than that in oxygen at 1200°C.

Table 2 Parabolic oxidation rate coefficients k_p ($g^2 \cdot cm^{-4} \cdot s^{-1}$) for the four alloys

	HEA05	**HEA06**	**HEA07**	**HEA08**
1000°C-O_2	3.5×10^{-10}	-	-	-
1000°C-H_2O	3.1×10^{-11}	-	-	-
1200°C-O_2	1.8×10^{-8}	1.4×10^{-11}	6.9×10^{-10}	3.1×10^{-11}
1200°C-H_2O	6.1×10^{-10}	6.0×10^{-12}	5.9×10^{-10}	3.1×10^{-11}

3.2.2.2 Phase constitutions

Phase constitutions of the oxidized alloys both in oxygen and steam at 1000°C and 1200°C were investigated by XRD, and the results are shown in Fig. 6. Table 3 summarizes the corresponding phase compositions identified from the XRD patterns in Fig. 6. The main oxide phase for each sample was also marked in the table.

As seen from Fig. 6 and Table 3, the recognizable difference in oxidation resistance of HEA05 in oxygen and steam originates from the dissimilar thermally grown oxide phases. In oxygen, only Mn_3O_4 but with two different crystal structures (α-Mn_3O_4: hausmannite, tetragonal; β-Mn_3O_4: cubic) was observed. In comparison, oxidation in steam resulted in the growth of three different types of oxides, i.e. Mn_2AlO_4, $MnAl_2O_4$ and Al_2O_3. In addition, the main phase altered from Mn_2AlO_4 at 1000°C to $MnAl_2O_4$ at 1200°C. The formation of a presumably protective Al_2O_3 layer can elucidate the remarkably improved oxidation resistance of HEA05 in steam. The different scaling behaviors for HEA05 in oxygen and steam can be rationalized by the different oxygen partial pressures in the two atmospheres, which will be discussed later.

In case of the other three alloys, same oxide phase constitutions were seen for each alloy after oxidation at both temperatures and atmospheres. At 1000°C, the FCC phase from the alloy substrate was also detected owing to the thinner oxide layers on the surface. For HEA06, only Al_2O_3 was detected as the oxide phase. The oxide layers are predominantly composed of $Fe(CoCrAl)_2O_4$ with small amount of Cr_2O_3 and Al_2O_3 for HEA07 with Zr addition. The phase compositions consist of Al_2O_3 (main phase) and $Fe(CoCrAl)_2O_4$ for HEA08 with Y addition. But the intensities of diffraction peaks of $Fe(CoCrAl)_2O_4$ are quite low.

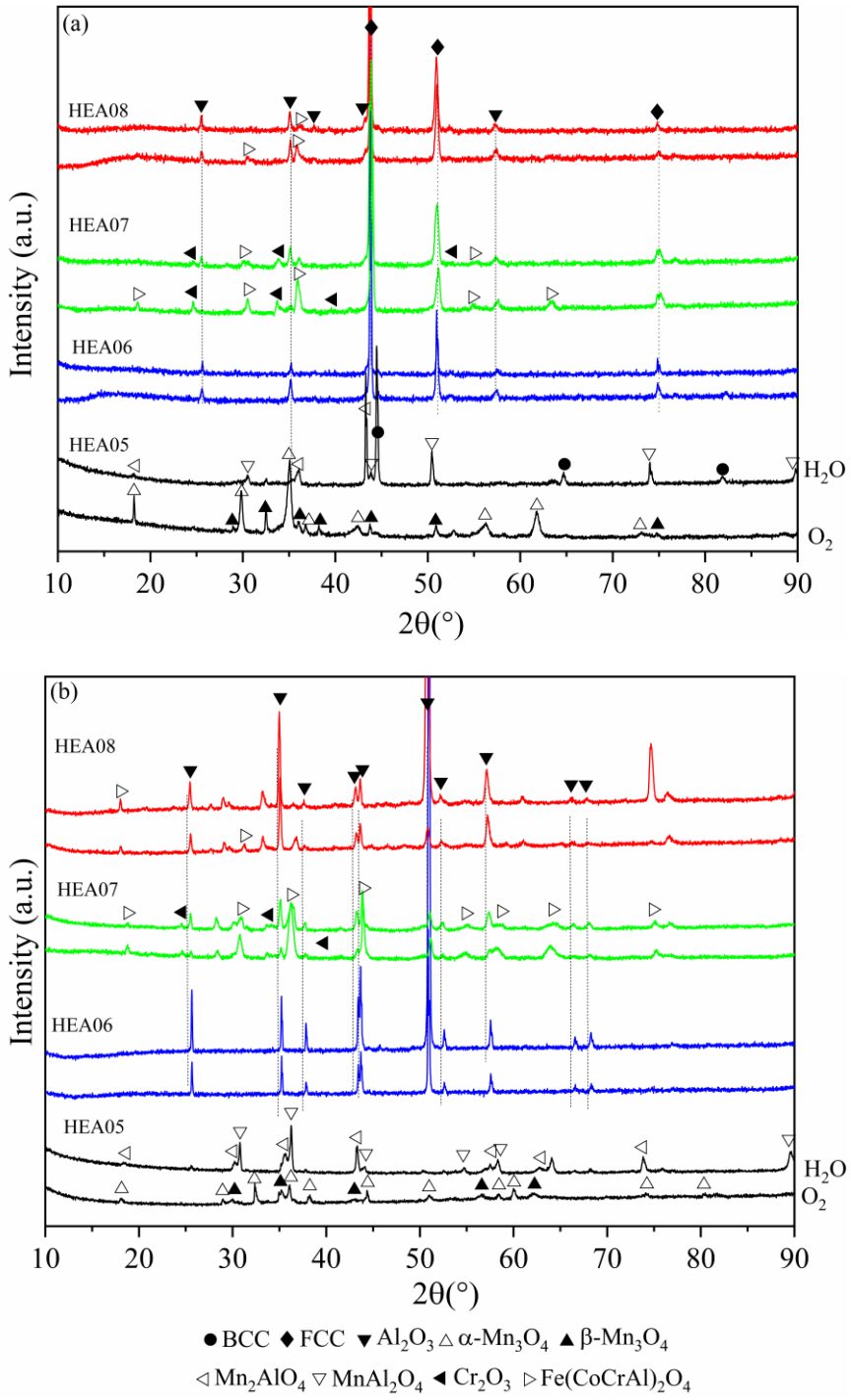

Fig. 6. XRD patterns of the four alloys after isothermal oxidation, (a) 1000°C and (b) 1200°C.

Table 3. Phases identified for the four alloys after isothermal oxidation by XRD

	HEA05	HEA06	HEA07	HEA08
1000°C-O_2	α-Mn_3O_4 (main) β-Mn_3O_4	Al_2O_3 (main) FCC	$Fe(CoCrAl)_2O_4$ (main) Cr_2O_3 Al_2O_3 FCC	Al_2O_3 (main) $Fe(CoCrAl)_2O_4$ FCC
1000°C-H_2O	Mn_2AlO_4 (main) $MnAl_2O_4$ Al_2O_3 BCC	Al_2O_3 (main) FCC	$Fe(CoCrAl)_2O_4$ (main) Cr_2O_3 Al_2O_3 FCC	Al_2O_3 (main) $Fe(CoCrAl)_2O_4$ FCC
1200°C-O_2	α-Mn_3O_4 (main) β-Mn_3O_4	Al_2O_3 (main)	$Fe(CoCrAl)_2O_4$ (main) Cr_2O_3 Al_2O_3	Al_2O_3 (main) $Fe(CoCrAl)_2O_4$
1200°C-H_2O	Mn_2AlO_4 $MnAl_2O_4$ (main) Al_2O_3	Al_2O_3 (main)	$Fe(CoCrAl)_2O_4$ (main) Cr_2O_3 Al_2O_3	Al_2O_3 (main) $Fe(CoCrAl)_2O_4$

3.2.2.3 Surface morphology

In order to intuitively describe the oxide scale configurations and elucidate the oxidation mechanisms of the four HEA alloys, detailed surface and cross-sectional microstructures were investigated by SEM combined with EDS examination. To simplify, only the results at 1200°C will be shown since similar oxidation behavior were seen at lower temperature 1000°C.

Fig. 7 shows the typical surface view of the alloys after oxidation test at 1200°C. A thick and discontinues oxide layer with significant peel off was seen on HEA05 after oxidation in oxygen. EDS analyses confirmed that major areas are rich in Mn and O, whereas in the regions where the outer layer peeled off exposing the interior layer contain more Cr and Al. These findings indicate that the oxide scale is mainly composed of Mn_3O_4 (according to XRD results) with internal oxidation of Cr and Al (see following cross section characterizations). In steam, the oxide scale becomes more convoluted and contains high contents of both Mn and Al in addition to O.

In both atmospheres, the HEA06 alloy formed a thin alumina scale, which then spalled off locally during cooling period, revealing the bulk material. HEA07 exhibited an external oxide scale rich in Fe, Co and Cr in both atmospheres, moreover with higher level of spallation in steam. In combination with XRD results in Table 3, it suggests that a surface layer of $Fe(CoAlCr)_2O_4$ grew. In addition, white particles rich in Zr were found on the surface at high magnification. Compared to HEA06, doping of Zr here alter the oxidation mechanism of the alloy without formation of an external, protective alumina scale. The surface of HEA08 shows a continuous oxide scale, containing Al and O in both atmospheres. There was no macroscopic evidences of scale spallation, but at high magnification microscale spallation of limited surface regions was observed in both atmospheres. Obviously, the adherence of the oxide scale was significantly improved by doping with Y. Similar to HEA07, reactive element (Y)-rich oxide particles were observed to nucleate and grow on the surface. In steam, some Y and Al rich large nodules were also seen on the surface as shown in Fig. 7. Their chemical compositions measured by EDS are close to

$Y_3Al_5O_{12}$ (YAG). These nodules are mainly formed on top of the initial Y-containing precipitates formed in the as-cast alloys (see following cross section). The formation of such nodules are likely related with steam enhancing the outward diffusion and segregations of Y on the surface during oxidation [39]. In addition, in the regions where the oxide scale still attached, no Ni-enrichment particles were found on the surface by EDS measurements for all four alloys. The measured Ni concentrations are usually below 1 at.%, which approaches the accuracy limit of the EDS.

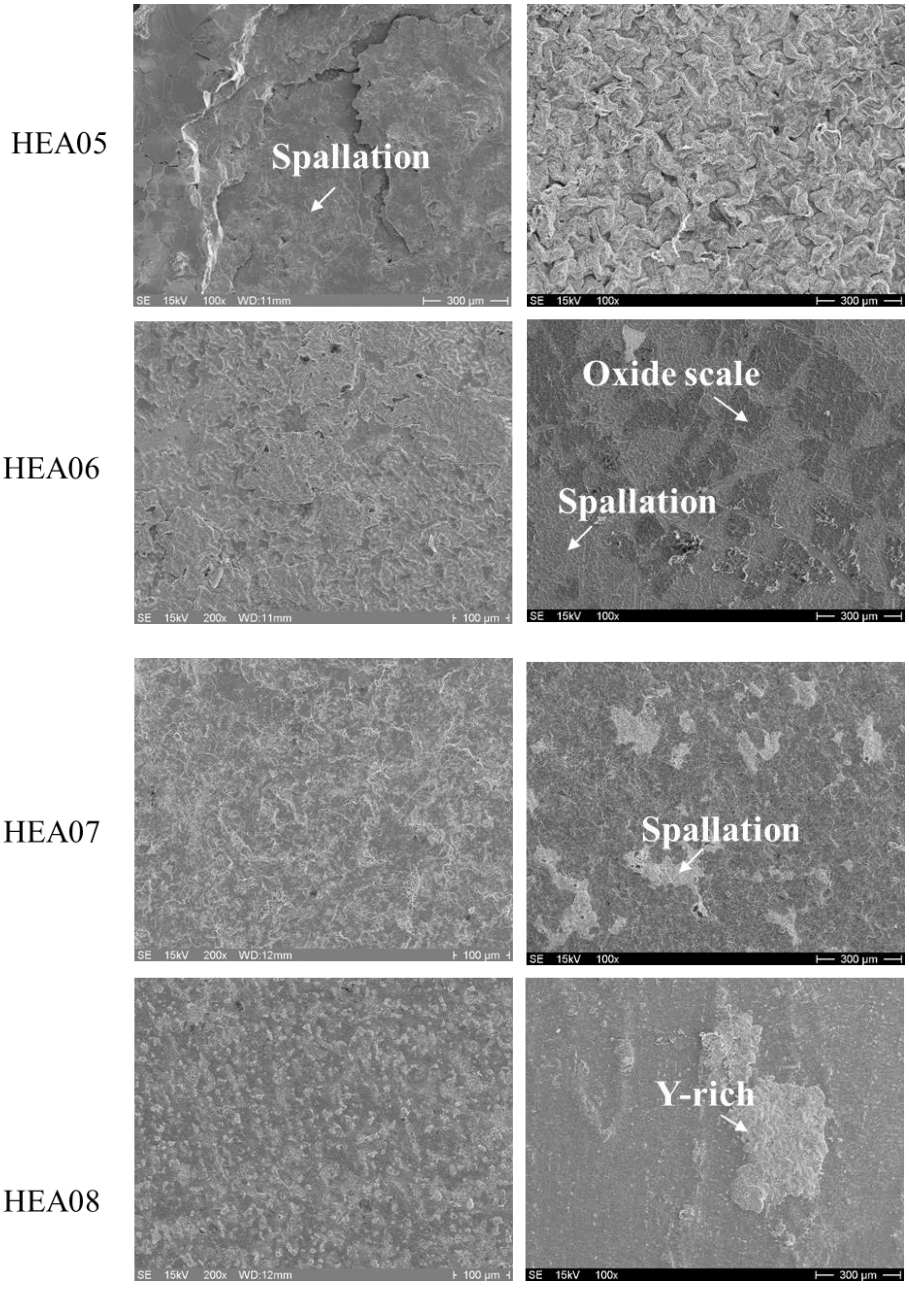

Fig. 7. SEM images displaying the surface morphologies of the alloys after isothermal oxidation at 1200°C. Left column: in oxygen, right column: in steam.

3.2.2.4 Cross section microstructure

Fig. 8 and Fig. 9 are the SEM images displaying the overview cross-sectional structure of the alloys after oxidation at 1200°C in oxygen and in steam, respectively. In accordance with XRD results, the thermally grown oxide scales of different layered configurations and chemical compositions were detected on HEA05 (containing Mn) after oxidation in oxygen and in steam, Fig. 8 (a) and Fig. 9 (a). All other three alloys (with Mn replaced by Co) demonstrated similar oxidation mechanisms with virtually identical oxide scale configurations in both atmospheres.

Fig. 10 displays the corresponding EDS mapping results of HEA05 after oxidation at 1200°C in oxygen. As can be seen in Fig. 8 (a) and Fig. 10, the oxide scale is mainly composed of an extremely thick (several hundred microns) Mn_3O_4 layer. This layer shows low coherence and adherence with substantial delamination and spallation. Beneath the Mn_3O_4 layer, internal oxidation of Cr and Al occurred owing to decreased partial pressure of oxygen and high thermodynamic stability of Cr_2O_3 and Al_2O_3. However, the internal oxidation did not establish a continuous protective layer based on Cr_2O_3 and Al_2O_3, and it suggests that Mn atoms can easily diffuse outwardly to be oxidized. In addition, the oxide/alloy interface was rather rough with large oxide protrusions. These observations evidence that oxidation of HEA05 in oxygen proceeds with both inward diffusion of anions (oxygen) and outward diffusion of cations (Mn) with high oxidation rates.

In comparison, oxidation of HEA05 in steam resulted in formation of an oxide scale with a triple-layered structure, Fig. 9 (a) and Fig. 11. More specifically, the oxide scale consist of a Mn_2AlO_4 spinel outer layer, a $MnAl_2O_4$ spinel intermediate layer and a continuous Al_2O_3 inner layer. This specific layered arrangement was proved by the EDS line-scanning and mapping results across the oxide layer in Fig. 11, and validated by the XRD result. The growth of Al_2O_3-based, multilayered oxide scale herein is associated with reduced oxygen partial pressure in steam and continuously decreasing oxygen partial pressure from the atmosphere to alloy matrix, which will be discussed later. Consequently, the growth of the continuous Al_2O_3 inner layer accounts for the remarkably improved oxidation resistance and reduced oxidation rate of the HEA05 in steam. Again, the oxide scale also showed low adherence with noticeable spallation.

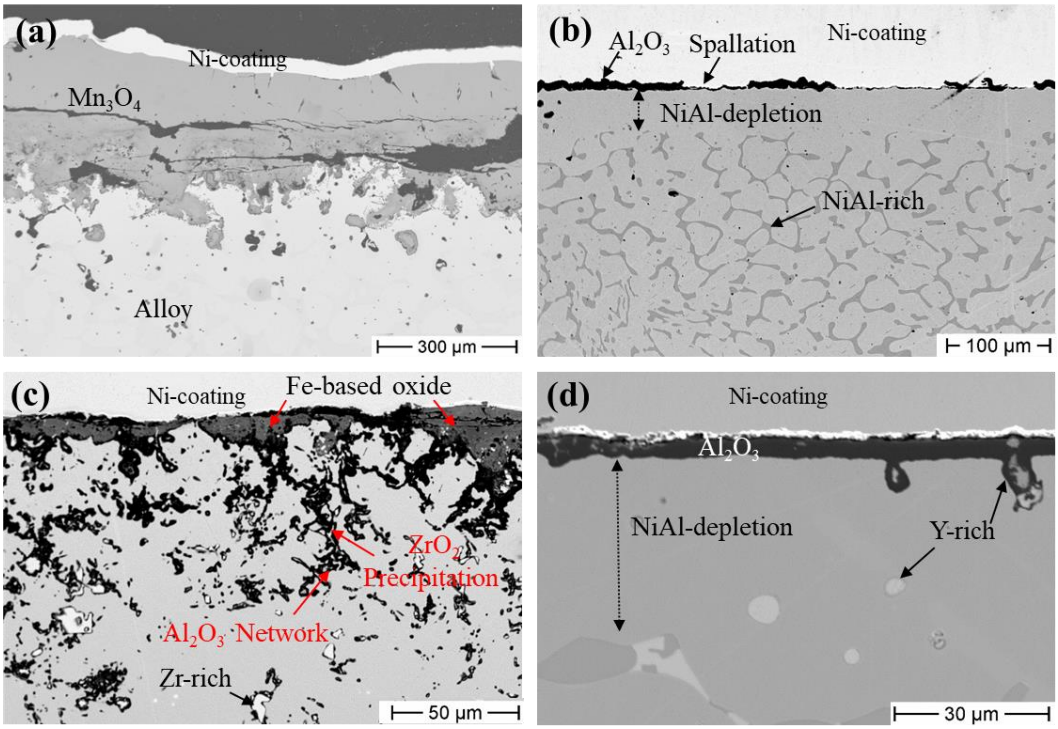

Fig. 8. Overview cross section structure of the alloys after isothermal oxidation at 1200°C in oxygen. (a) HEA05, (b) HEA06, (c) HEA07, (d) HEA08.

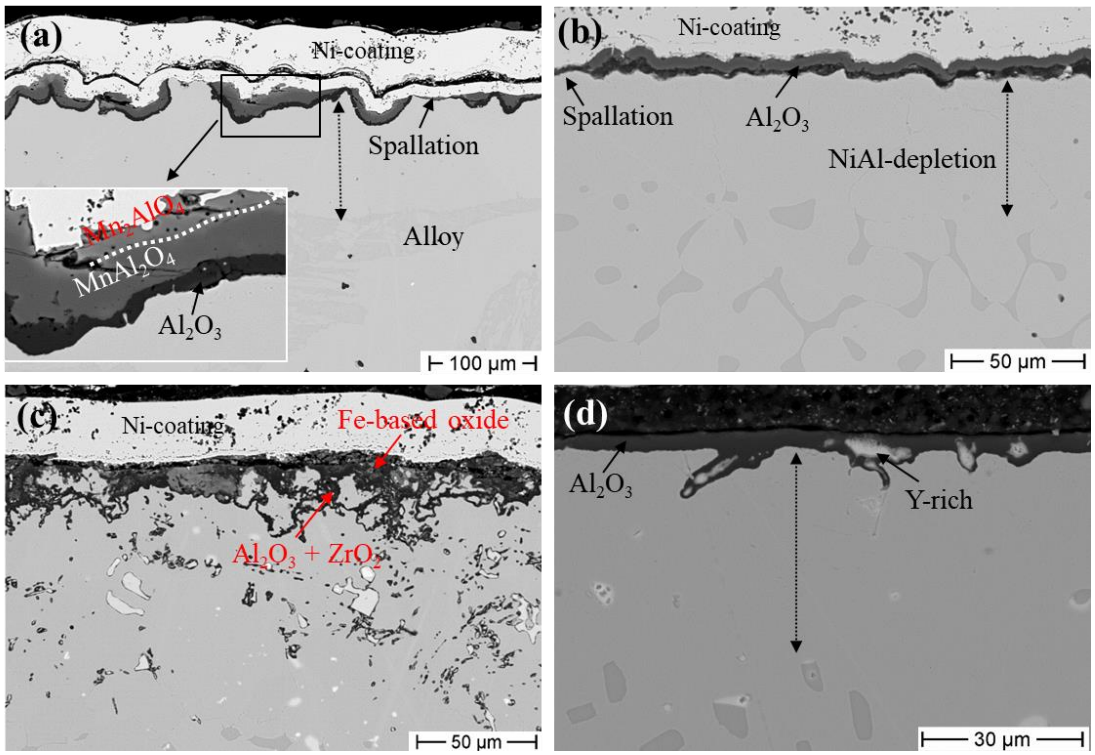

Fig. 9. Overview cross section structure of the alloys after isothermal oxidation at 1200°C in steam. (a) HEA05, (b) HEA06, (c) HEA07, (d) HEA08.

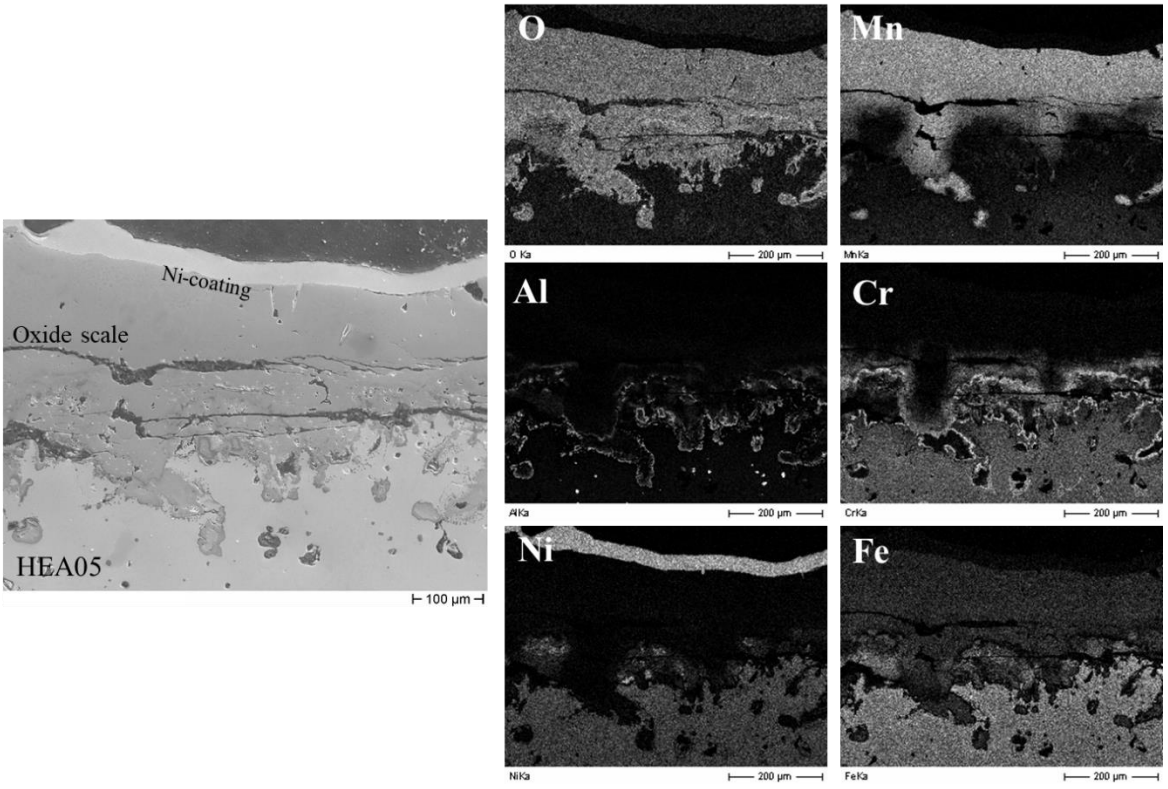

Fig. 10. Cross section SEM image and corresponding EDS mapping graphs of HEA05 after isothermal oxidation at 1200°C in oxygen.

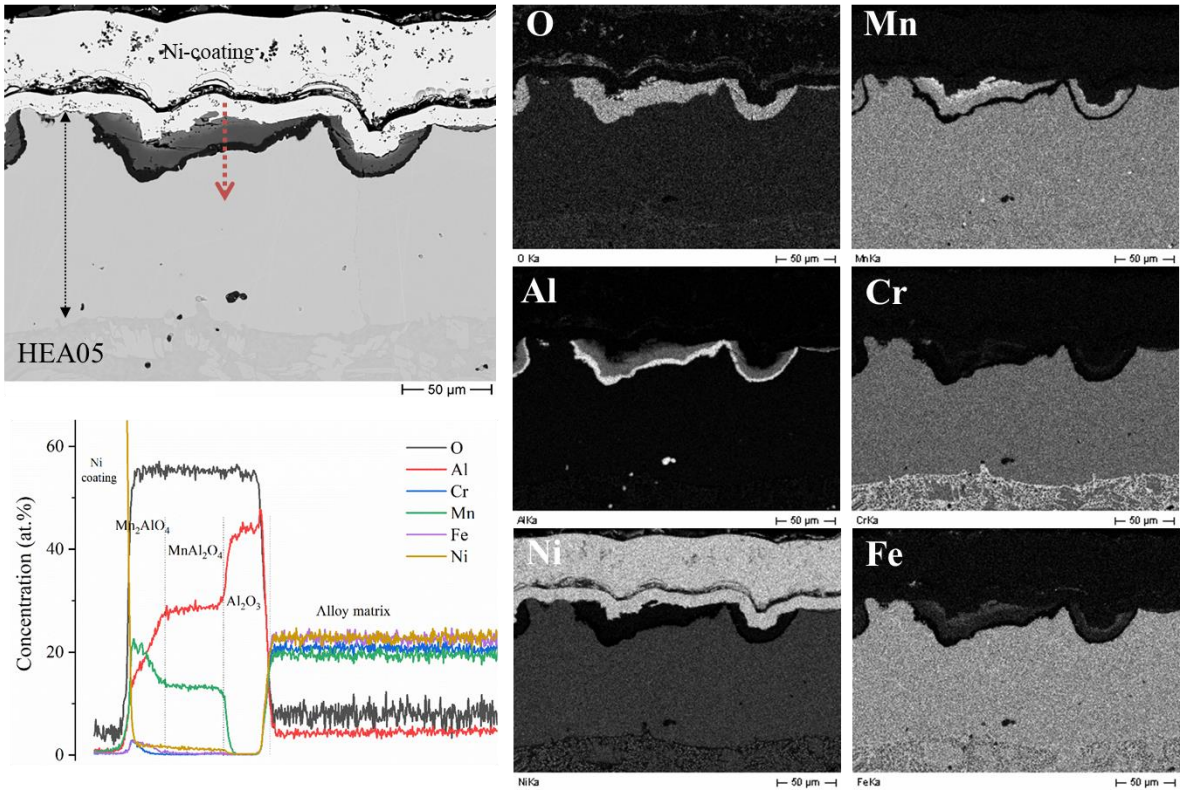

Fig. 11. Cross section SEM image and corresponding EDS mapping graphs and line scanning along the arrow of HEA05 after isothermal oxidation at 1200°C in steam.

Fig. 12 illustrates the cross-sectional microstructure and corresponding EDS mapping graphs of HEA06 after oxidation at 1200°C in oxygen. Combined Fig. 8 (b), Fig. 9 (b) and Fig. 12, it is undoubtedly confirmed that selective oxidation of Al occurred for HEA06 in both atmospheres, resulting in growth of a thin and protective alumina scale with a single-layer structure during high temperature exposure. The oxide scales revealed a convoluted morphology, caused by the oxidation induced growth and thermal stresses and their relaxation process, which are typically seen for high-temperature oxidation of alumina-forming alloys without reactive element addition [40]. The oxide scales show low adhesion to the alloy substrate with significant spallation. The spallation was initiated during cooling stages since no sign of oxidation or oxide layer was seen on where the scales have peeled off.

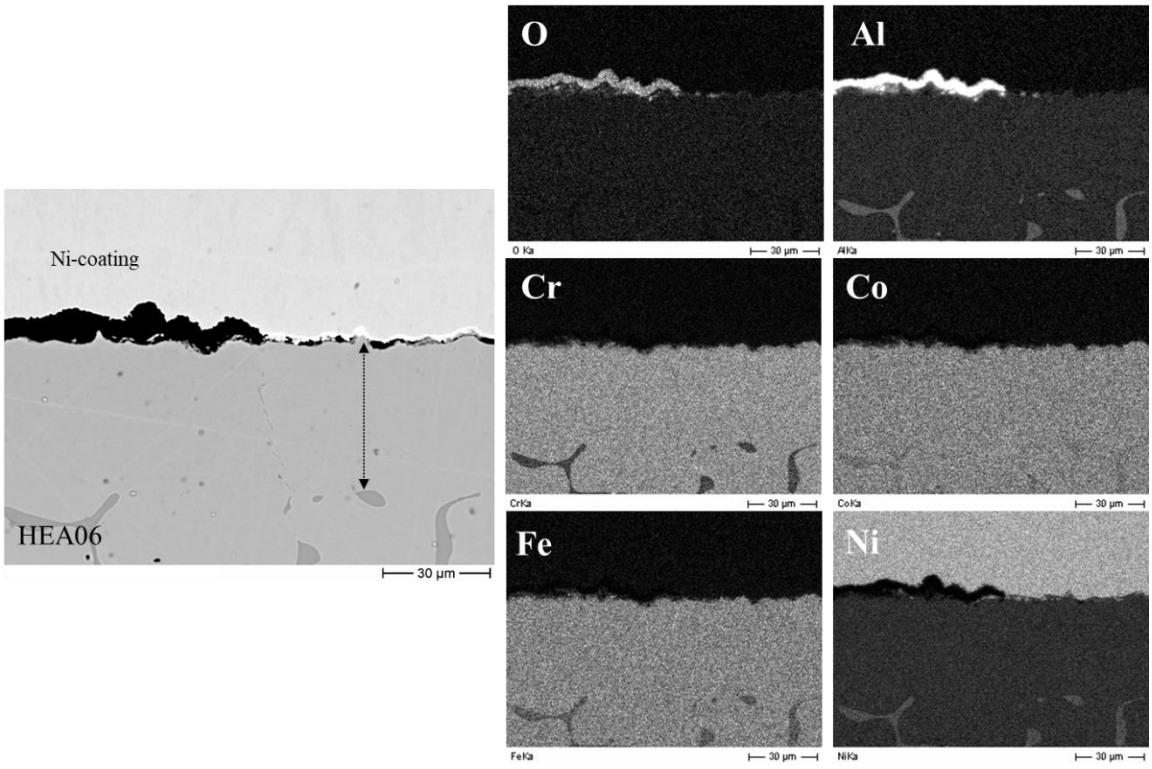

Fig. 12. Cross section SEM image and corresponding EDS mapping graphs of HEA06 after isothermal oxidation at 1200°C in oxygen.

On the HEA07 with 1 wt.% Zr addition compared to HEA06, the thermally grown oxide scales now presented a bi-layered morphology in both atmospheres, consisting of a thick $Fe(CoCrAl)_2O_4$ spinel outer layer and a thin Cr_2O_3 + Al_2O_3 (main phase) inner layer, as proved by Fig. 8 (c), Fig. 9 (c) and EDS mapping results in Fig. 13. In addition, the segregation of Zr at grain boundaries, Fig. 2 (c), serves as short circuit diffusion paths for oxidizing species, leading to internal oxidation and formation of Al_2O_3 network mainly along grain boundaries within the alloy matrix. Simultaneously, Zr was also oxidized and incorporated into the alumina network as ZrO_2, Fig. 13. The relatively high level of dopant in metallic form (Zr herein) leads to the over-doping phenomenon with excessive internal oxidation, which likely overshadow the beneficial reactive element (RE) effect on enhanced Al selective oxidation and improved scale adherence [41]. The

underlying mechanisms of Al_2O_3 network formation is mainly connected with high solubility of oxygen in metallic zirconium and the high diffusivity of oxygen ions in ZrO_2 [42,43] (see discussion part).

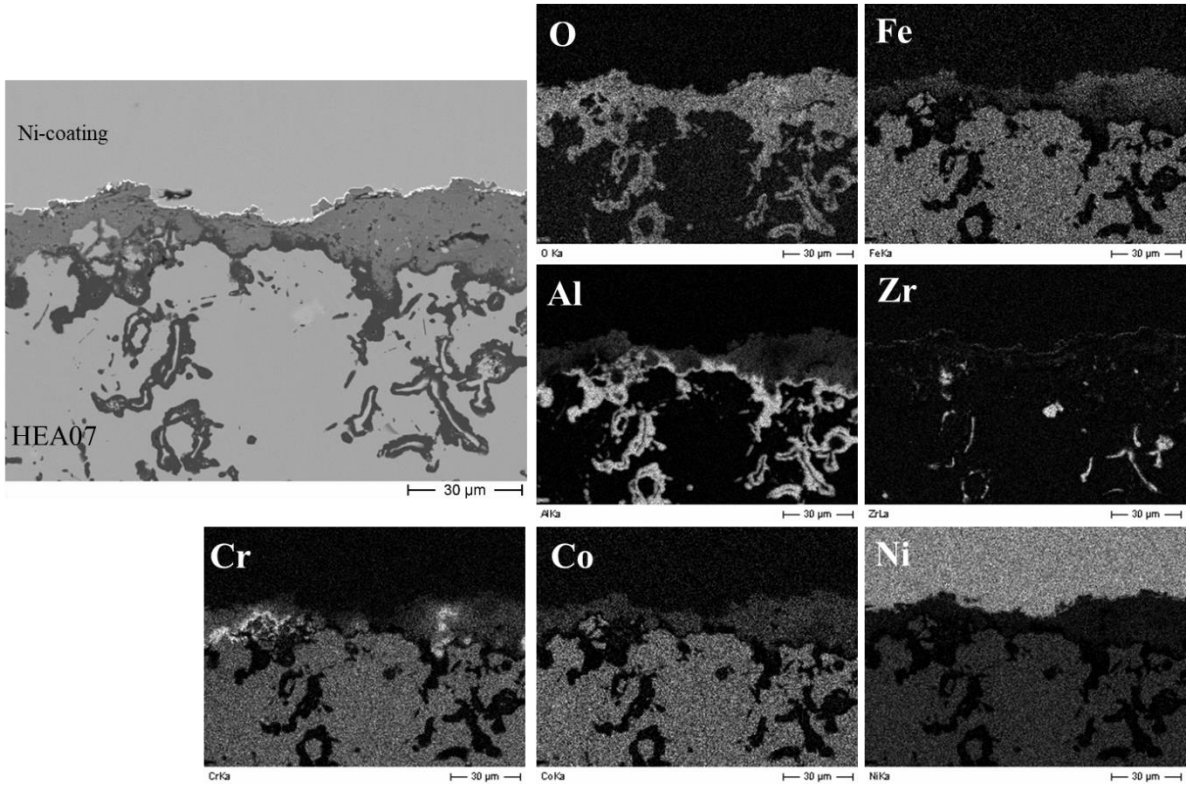

Fig. 13. Cross section SEM image and corresponding EDS mapping graphs of HEA07 after isothermal oxidation at 1200°C in oxygen.

Fig. 14 shows the cross-sectional microstructure and corresponding EDS line-scanning results of HEA08 after oxidation at 1200°C in oxygen. As seen in Fig. 8 (d), Fig. 9 (d) and Fig. 14, selective oxidation of Al occurred in HEA08 with a thermally grown, thin and dense alumina scale in both atmospheres. In addition, the EDS line-scanning results in Fig. 14 reveal that a superficial layer rich of Fe, Co, Cr, Y formed above the alumina layer. The presence of Fe, Co, Cr elements was related with the $Fe(CoCrAl)_2O_4$ phase identified by XRD, most probably owing to the initial transient oxidation stage before establishment of the continuous alumina scale [38]. This layer is prone to spallation that accounts for the microscale spallation observed during surface examinations. Surface and grain boundary segregations of Y-rich oxide within the alumina scale was further confirmed here. No obvious internal oxidation was seen here compared to HEA07 with Zr addition. Contrary to the oxide scales showing convoluted morphology with low adherence on the other three alloys, the alumina scales on HEA08 demonstrated considerably more uniform and smooth structure without scale exfoliation except with some Y-rich oxide protrusions at the scale/alloy interface. The beneficial reactive element effect, principally including improved adherence and suppression of convoluted structure formation for alumina scale, was unraveled for the Y-doping HEAs oxidation at elevated temperatures.

A NiAl-rich BCC phase depletion zone beneath the oxide scale, except for HEA05 oxidized in oxygen, as shown in Fig. 8 - Fig. 14 with the dashed arrow lines was seen. The depth of the depletion zone varied from ~ 45 μm for HEA06 and HEA08 to ~ 95 μm for HEA05 and HEA07. The NiAl-rich phase acts as main Al reservoir for alumina scale formation during oxidation, which dissociates after outward diffusion and selective oxidation of Al. The thicker depletion zones for HEA05 and HEA07 can be attributed to their faster oxidation rates and thicker oxide scale growth. The alloy matrix after oxidation maintained their microstructural stability with the original duplex phase composition.

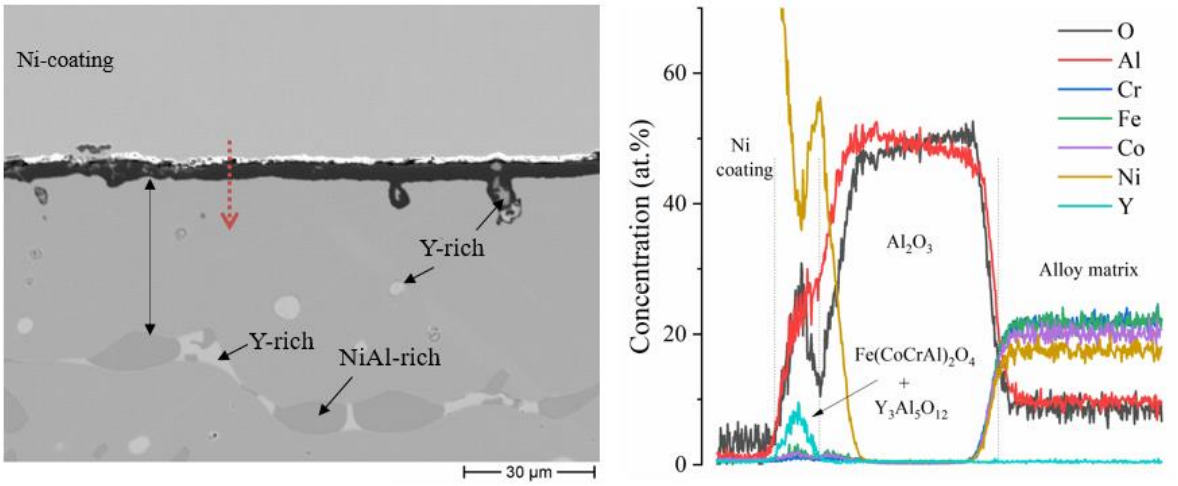

Fig. 14. Cross section SEM image and corresponding EDS line scanning along the arrow of HEA08 after isothermal oxidation at 1200°C in oxygen.

4. Discussion

4.1 Effect of principal alloying elements and oxidizing atmospheres

Oxidation of the four HEAs discloses that the oxidation behavior of Mn-containing alloys is susceptible to oxidizing atmospheres, more specifically to the oxygen partial pressure. However, the Co containing alloys, characterized by protective alumina scale formation, are not evidently influenced by the oxidizing atmosphere, i.e. oxygen or steam herein. These dissimilar oxidation phenomena depending on the principal alloying elements and the oxidizing atmospheres can be rationalized by the thermodynamic stability and the equilibrium oxygen partial pressure of various oxides.

Fig. 15 presents the Gibbs free energy of formation for some selected oxides (i.e. Ellingham diagrams [44]) involved in this study. Even though the diagrams are plotted with pure metals (in the real case the chemical activity of each element, for example in the HEAs, are different), they are very useful to predict and understand the oxidation behavior of materials related to different atmospheres. The lower Gibbs free energy implies the higher thermodynamic stability of the oxide with lower equilibrium oxygen partial pressure, which will be subject to preferential oxidation (assuming identical chemical activity) in an oxidizing atmosphere. In addition, transition elements generally exhibit variable valency and they can form several types of oxides with different stoichiometry, such as the Co, Fe and Mn elements shown in Fig. 15. Oxidation of these elements to form a specific type of oxide commonly depends on the oxygen partial pressure in the oxidizing atmosphere.

As seen in Fig. 15, apart from the reactive elements (Zr and Y), the stability of oxides follows the sequence of Cr_2O_3, MnO and Al_2O_3. In case of HEA05 oxidized in oxygen, the high oxygen partial pressure (1 atm here) and half atomic concentration of Al compared to Mn can promote the preferential oxidation of Mn. According to Fig. 15, MnO will be the preferentially formed oxidation product initially. However, MnO, the lowest valence oxide of manganese, can pick up oxygen and be further oxidized easily even at room temperature [45]. Thus, growth of a higher valence manganese oxide, i.e. Mn_3O_4, can be anticipated. This is consistent with experimental observations, as seen in Fig. 10. Previous studies found that HEAs own typically sluggish diffusion behavior, but with higher diffusion coefficients of Mn than those of, for example Cr, Fe, Ni and Co [46]. Therefore, one could expect that oxidation of HEA05 in oxygen proceeds with continuous, fast outward diffusion of Mn cations, resulting in a porous and non-protective Mn_3O_4 layer. Inward diffusion of oxygen anions can also occur owing to the porous feature of the Mn_3O_4 layer with an uneven scale/alloy interface. A weak internal oxidation of Cr and Al was also seen beneath the thick Mn_3O_4 layer, Fig. 10, because of diminished oxygen partial pressure at oxide/alloy interface. It is suggested that the porous Mn_3O_4 layer cannot substantially reduce the oxygen partial pressure at scale/alloy interface to promote the formation of a continuous Cr_2O_3 or Al_2O_3 based layer via internal oxidation. Thus, oxidation of HEA05 in oxygen at high temperatures proceeds with the fast growth of porous Mn_3O_4 scale.

In a pure steam atmosphere, the oxygen partial pressure will be determined by the dissociation of H_2O. Thus, a remarkably lower oxygen partial pressure will be present in steam (in the magnitude of ~10^{-5} atm at 1200°C) compared to that in oxygen (1 atm). The much lower oxygen partial pressure likely initiates both oxidations of Mn and Al for HEA05 in steam. In the Mn-Al-O system, there exist two types of solid-solution spinel phases ($Mn_{3-x}Al_xO_4$, x: 0-2): tetragonal and cubic [47]. The cubic phase represents a thermodynamic stable phase at high temperatures, and the cubic Mn_3O_4 phase can extend up to $MnAl_2O_4$ [48]. Fig. 16 shows the calculated Mn–Al–O phase diagrams at 1200°C with molar metal ratio versus equilibrium oxygen partial pressure. Formation of cubic spinel oxides is predicted at oxygen partial pressure of ~10^{-5} atm and Mn : Al molar ratio of 2. During the initial oxidation stage, oxidation of Mn can dominate the oxidation process because of the higher concentration of Mn within the alloys. As a consequence, Mn-rich oxide layer Mn_2AlO_4, as proved by XRD and EDS, firstly establishes on the alloy surface. As the oxygen partial pressure gradually decreases from the gas/scale interface to scale/alloy interface, the dominantly oxidizing species will alter from Mn to Al with oxide scale thickening since alumina possesses higher thermodynamic stability and lower equilibrium oxygen partial pressure than manganese oxides, as shown in Fig. 15. The oxide formation altering from solid-solution spinel to corundum (alumina) with decreasing oxygen partial pressure is also confirmed by Fig. 16. As the oxidation proceeds, a triple-layered oxide scale finally grows with a middle $MnAl_2O_4$ layer and an interior Al_2O_3 layer. It is necessary to mention that the composition of the spinel oxide layer may successively alter from Mn_2AlO_4 to $MnAl_2O_4$ as seen in Fig. 11 of EDS line-scanning results. Their similar crystal structure and lattice parameters make it difficult to distinguish via XRD measurement. Compared to the single Mn_3O_4 layer formed in oxygen, the multilayered oxide scale herein consisting of spinel and alumina shows much denser microstructure and lower ions diffusion rates. Therefore, the outward diffusion of cations will be greatly suppressed and the oxidation mechanisms will be predominantly inward diffusion of anions in steam, with significantly improved oxidation resistance. The findings herein indicate that pre-oxidation of the Mn-containing HEA05 in low oxygen partial pressure atmosphere (e.g. using H_2O-H_2 mixture) can improve its oxidation resistance for high-temperature applications.

As seen in Fig. 15, the Ni-, Co-, and Fe-oxides demonstrate much lower thermodynamic stability and higher dissociation partial pressures of oxygen than Cr_2O_3 and Al_2O_3. Their equilibrium oxygen partial pressures are comparable to that of steam. Therefore, Al and Cr will be preferentially oxidized for HEA06 (AlCrFeNiCo) when exposed to high temperature oxidizing atmospheres. Moreover, it is well recognized that chromium, acting as a third element and secondary getter for oxygen in FeCrAl or NiCrAl alloys (third element effect), can enhance the selective oxidation of Al leading to alumina scale formation in alloys with lower Al concentration [49–51]. Growth of an external alumina scale have been frequently reported during high-temperature oxidation of FeCrAl alloys with 20.wt% Cr and Al concentration reaching only ~3 wt.% [52]. The presence of chromium in such HEAs apparently can act similarly. As expected, selective oxidation of Al occurs for HEA06 at elevated temperatures in both oxygen and steam atmospheres. Previous studies also concluded that steam or water vapor had little effect on the oxidation kinetics of alumina-forming alloys except some evidences indicate that scale adhesion is reduced [53]. Experimental results in this study confirm these findings, which shows very similar oxidation rates but higher levels of spallation after oxidation in steam.

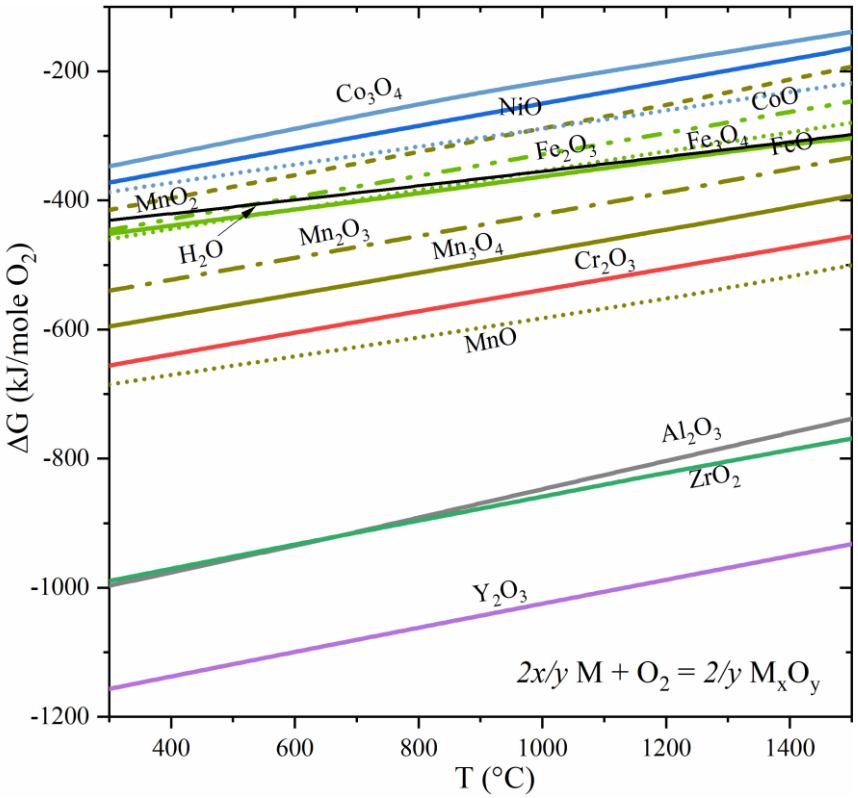

Fig. 15. Gibbs free energy of formation of some selected oxides (i.e. Ellingham diagrams) calculated by HSC Chemistry 9 showing their thermodynamic stability.

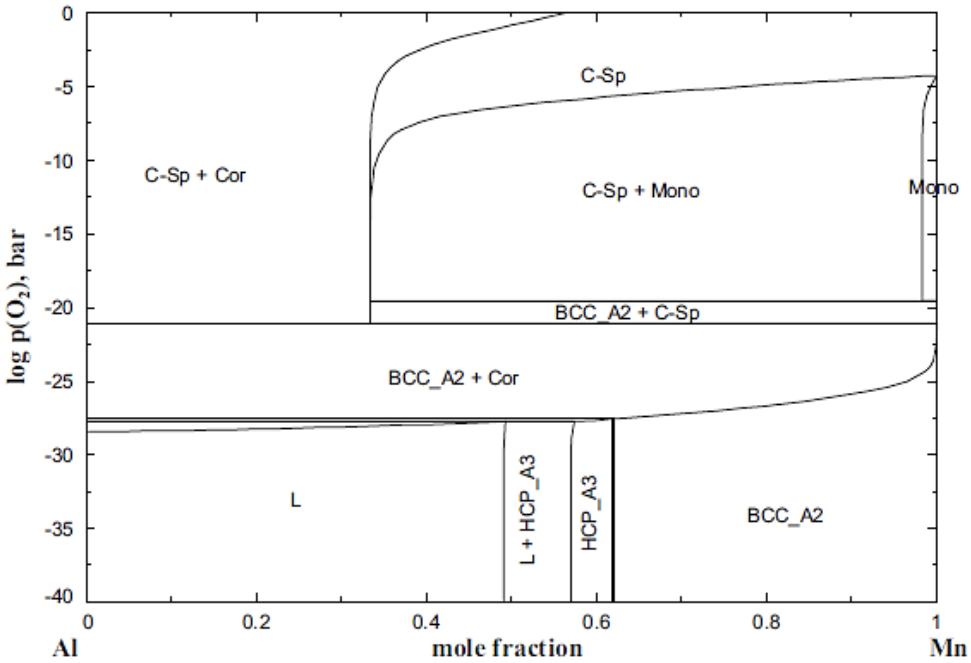

Fig. 16. Calculated Mn–Al–O phase diagrams at 1200°C. Molar metal ratio versus equilibrium oxygen partial pressure. L: liquid, C-Sp: $Mn_{3-x}Al_xO_4$ cubic spinel, Mono: monoxide, Cor: corundum. [48]

4.2 Effect of reactive elements

Small additions of so-called reactive elements (RE), e.g., Y, Zr, Hf, and Ce, either in elemental form or dispersed RE oxide particles, to enhance the oxidation performance and lifespan of alumina-forming high-temperature alloys have been widely documented and studied [33,41,54,55]. The beneficial effects for RE addition include remarkably improved scale adherence, suppression of convoluted oxide scale morphology and void formation, enhanced selective Al oxidation and altering scale growth mechanism from both anion and cation to predominant anion diffusion. During oxidation, RE ions will segregated at oxide scale grain boundaries and the metal/scale interface. Additionally, elemental additions of RE within the alloy must maintain at a low level (less than 1 wt.%, typically ~0.3 wt.%) since over-doping will result in undesirable excessive internal oxidation of RE and Al inside the alloy matrix [55] since their oxides also possess high thermodynamic stability with low equilibrium oxygen partial pressures, Fig. 15.

The two most common reactive elements, i.e. Zr and Y, were considered in this study; however, different outcomes were observed as presented in the results section. Even though the concentration of this two elements were identical (1 wt.%), it suggests that such level of Zr addition already leads to the over-doping effect [56]. The relatively high level of Zr dopant cannot offer any beneficial effects and even deteriorates the oxidation resistance of the alloys (HEA07) compared to un-doped one (HEA06). The oxide scale on HEA07 consists of an outer porous Fe-based spinel layer and an inner Al_2O_3 layer with substantial internal oxidation of Al and Zr. However, the aforementioned beneficial effects were affirmed for the yttrium doped alloys (HEA08). The thermally grown alumina oxide scales in both atmospheres display a smooth and compact morphology as well as high adherence. The dissimilar oxidation behaviors indicate that the doping level of Zr is more susceptible to excessive internal oxidation compare to that of Y. The conceivable explanations are associated with the different oxygen solubility in metallic Zr and Y, as well as different oxygen diffusivity in their oxides. It is well known that Zr can dissolve quite high amount of oxygen at elevated temperatures and the oxygen solubility reaches ~30 at.% at 1200°C [57]. In comparison, the oxygen solubility in metallic Y is relatively lower, around ~12 mol.% [58]. The higher solubility of oxygen in Zr may alter the solubility/concentration and diffusivity of oxygen in the alloy, and the addition of Zr within the alloy can also change the chemical activity and diffusivity of Al in the alloy [31,59]. Both hypotheses likely affect the initial stages of oxide nucleation and promote the growth of Fe-based mixed oxides. Segregation of the reactive element (Zr) at alloy grain boundaries results in internal oxidation and precipitation of ZrO_2, which provides short circuit diffusion path for oxygen since ZrO_2 can tolerate high level of defects mainly with oxygen vacancies and has high oxygen diffusivity [43,60]. In yttrium-doped alloys (HEA08), large Y-rich oxide protrusions formed in this study because of relatively high doping level and localized enrichment of Y-containing precipitates in the alloy. These oxide protrusions can induce localized stress concentration, promote nucleation of interfacial cracks and degrade the alumina scale adherence [27,41]. The formation of such large Y-rich oxide protrusions has to be diminished or eliminated, for instance by optimizing the doping level and dispersion morphology of REs, to maximize their oxidation performance.

A thin Fe-based spinel oxide layer was seen above the continuous alumina scale on HEA08, but not detected on HEA06 without Y addition. For Al_2O_3-forming multi-element materials, high temperature oxidation typically takes place via initial transient oxidation stage following by a steady state stage (growth and thickening of alumina scale) [61–63]. Transient oxidation involves growth of a thin surface layer consisting of more noble metal oxides and spinels with poor protective effect and higher oxidation rate. Similar transient oxidation phenomenon also has been observed during oxidation of HEA alloys [26,32]. For instance, oxidation of similar HEA with compositions $Al_{12}(CoCrFeNi)_{88}$ and $Al_{15}(CoCrFeNi)_{85}$ at lower temperatures in air detected a relatively thick $NiCr_2O_4$ and Cr_2O_3 outer layer on top of a continuous internal Al_2O_3 layer [32]. The growth of the thin Fe-based spinel oxide layer on HEA08 can be viewed as a consequence of initial transient oxidation. However, in this study absence of Ni-based oxides and much thinner Fe-based spinel oxide/ Cr_2O_3 layers were observed. The higher oxidation temperature here likely suppress such transient oxidation stage and promote fast growth of alumina layer. In addition, the lower adherence of the oxide scale and a weak interface between this spinel layer and the inner alumina layer likely lead to its substantially or completely peel off on HEA06 without Y addition. More experimental and theoretical work is needed to obtain a deep mechanistic understanding of RE addition on the oxidation behavior of the HEAs and their doping level/morphology also has to be optimized to achieve optimal oxidation performance [56].

4.3 Comparison of oxidation kinetics

Materials that are designed for applications in high-temperature oxidizing environments rely on the thermal growth of an external, protective oxide scale. The formation of Al_2O_3 scales is favorable especially for water vapor–containing atmospheres since alumina possesses high thermodynamic stability with negligible volatilization and slow growth rate [64–66]. To give some insights into the oxidation performances of the model HEAs herein, their oxidation kinetics at 1200°C are quantitatively compared with well-documented alumina-forming FeCrAl alloys and other HEAs with similar chemical compositions, and their parabolic oxidation rate constants are shown in Table 3. Previous studies on the oxidation of HEAs were mainly carried out in air atmosphere with temperatures below 1200°C [26,28,29,31–33], few studies targeting at higher temperatures focused on their scaling behavior without reported oxidation kinetics [27,66]. Therefore, the parabolic oxidation rate coefficients available at highest temperatures are included in the Table 4.

As displayed in Table 4, the oxidation rate coefficients of the two alumina-forming HEAs, with or without Y addition, exhibit the same order of magnitude as those of FeCrAl alloys, which proves their excellent oxidation resistance even at very high temperature (1200°C) in both oxygen and steam atmospheres. Doping of Y can slightly reduce the oxidation rate of FeCrAl alloys compared to undoped ones. While, the doped HEA08 yields slightly higher oxidation rates compared to the undoped HEA06. The doping level in the FeCrAl alloys are typically maintained at a quite low level, below 0.1 wt.% [55,67]. However, the addition of Y was selected at a relatively higher level here, ~1 wt.%, to intuitively elucidate the RE effect. The slightly higher

oxidation rate thus can be attributed to the relatively higher level of Y addition with high amount of Al/Y oxide protrusions formation in this study (Fig. 14).

Previous studies on oxidation of other HEAs with analogous chemical compositions stated similar oxidation characteristics with comparable parabolic oxidation rate constants, Table 4. It is noteworthy to point out that their scaling behavior and oxidation kinetics also rely on the Al content with the alloys, similar to a variety of alumina-forming materials. A relatively low Al content will result in growth of a discontinuous Cr_2O_3 external scale with Al_2O_3 internal layer [26,32]. Increasing the Al content can promote the formation of a continuous, exclusive Al_2O_3 scale with reduced oxidation rate. Lu et al. recently reported that Y/Hf co-doped AlCoCrFeNi high-entropy alloy displayed superior oxidation performance with one magnitude lower oxidation rate than those of conventional NiCoCrAlY alloys at 1100°C and remarkable scale spallation resistance [33]. The underlying mechanisms governing the slow oxidation rate mainly relate with beneficial RE effects and larger columnar grain size of alumina oxide. Another favorable characteristic for HEAs is the reduced diffusivities of the alloying elements (and oxygen) compared to conventional structural alloys because of a reduced concentration of free vacancies, which likely further diminish their oxidation rates [31,46,68].

Table 4. Comparison of parabolic oxidation rate coefficients k_p ($g^2 \cdot cm^{-4} \cdot s^{-1}$) for various HEAs and FeCrAl alloys at 1200°C.

	Oxygen/Air	**Steam**	**Reference**
HEA06 ($Al_{0.5}$CrFeNiCo)	1.4×10^{-11}	6.0×10^{-12}	This study
HEA08($Al_{0.5}$CrFeNiCo+Y)	3.1×10^{-11}	3.1×10^{-11}	This study
FeCrAl	1.4×10^{-11}	1.0×10^{-11}	[55]
FeCrAl+Y	7.5×10^{-12}	7.9×10^{-11}	[55][67]
$Al_{0.3}$CoCrFeNi	1.7×10^{-12} (1100°C)	-	[28]
$Al_{0.7}$CoCrFeNi	3.8×10^{-13} (1100°C)	-	[28]
AlCoCrFeNi+YHf	1.9×10^{-13} (1100°C)	-	[33]
$Al_x(CoCrFeNi)_{100-x}$ x: 8-30	$\sim 10^{-13}$ - 10^{-11} (1050°C)	-	[32]

5. Conclusions

Four $Al_{0.5}$CrFeNi-(Mn or Co) based HEAs, with or without reactive element addition, have been produced. The effects of principal alloying element (Mn or Co), minor RE doping (Zr or Y), and oxidizing atmosphere (oxygen or steam) on their oxidation behaviors at 1000°C and 1200°C have been investigated. The main conclusions are summarized below.

(1) All four alloys solidified dendritically with dual phase constitutions, both BCC/B2 and FCC phases. The reactive element additive (Zr and Y) essentially segregates at boundaries of dendritic domains, limiting their coalescence and resulting in grain refinement effect.

(2) The $Al_{0.5}$CrFeNiMn alloy displayed poor oxidation resistance in air and different oxidation mechanisms in oxygen and steam. The oxide scales are composed of a thick Mn_3O_4 single layer in oxygen and a triple-layer assembly ($Mn_2AlO_4/MnAl_2O_4/Al_2O_3$) in steam with significant reduced oxidation rate, respectively. The different scaling behaviors in oxygen and steam can be attributed to the different oxygen partial pressures and preferential initial oxidation of Mn.

(3) Selective oxidation of Al occurs for $Al_{0.5}$CrFeNiCo alloys during oxidation in both oxygen and steam atmospheres, forming an external, dense and protective alumina scale. The oxidation kinetics are comparable to alumina-forming FeCrAl alloys, indicating its excellent high-temperature oxidation resistance. However, the oxide scales displayed low adherence with significant peeling off during cooling.

(4) Doping of Zr or Y (~1 wt.%) to $Al_{0.5}$CrFeNiCo alloys resulted in converse outputs on their oxidation performances. Addition of 1 wt.% Zr already yields the over-doping effect, deteriorating its oxidation resistance and changing the oxide scale structure from a single, external Al_2O_3 scale to Fe-based spinel/Al_2O_3 bi-layered oxide scale with substantial Al+Zr internal oxidation. The plausible explanations are associated with high oxygen solubility and oxygen diffusivity in metallic Zr and Zr oxides, respectively. The beneficial RE effects of Y addition are confirmed by means of remarkably improved oxide scale adherence and suppression of convoluted oxide scale morphology.

Overall, via optimizing the Al concentration (to balance oxidation resistance and mechanical properties [25]), doping species and their doping level, these alumina-forming HEAs demonstrate great promise for high-temperature applications in harsh environments.

Conflicts of interest

The authors declare that they have no known competing financial interests or personal relationships that could have appeared to influence the work reported in this paper.

Data availability

The datasets obtained during the current study are available from the corresponding author on reasonable request.

Acknowledgements

The authors thank Justine Poncelet for performing majority of the oxidation test. This work was supported by the Helmholtz program NUSAFE at the Karlsruhe Institute of Technology.

Reference

[1] J.C. Williams, E.A. Starke, Progress in structural materials for aerospace systems, Acta Mater. 51 (2003) 5775–5799. https://doi.org/10.1016/j.actamat.2003.08.023.

[2] S.J. Zinkle, J.T. Busby, Structural materials for fission & fusion energy, Mater. Today. 12 (2009) 12–19. https://doi.org/10.1016/S1369-7021(09)70294-9.

[3] M. Schütze, W.J. Quadakkers, Future Directions in the Field of High-Temperature Corrosion Research, Oxid. Met. 87 (2017) 681–704. https://doi.org/10.1007/s11085-017-9719-3.

[4] Z. Sun, H. Bei, Y. Yamamoto, Microstructural control of FeCrAl alloys using Mo and Nb additions, Mater. Charact. 132 (2017) 126–131. https://doi.org/10.1016/j.matchar.2017.08.008.

[5] S. Dryepondt, K.A. Unocic, D.T. Hoelzer, C.P. Massey, B.A. Pint, Development of low-Cr ODS FeCrAl alloys for accident-tolerant fuel cladding, J. Nucl. Mater. 501 (2018) 59–71. https://doi.org/10.1016/j.jnucmat.2017.12.035.

[6] J.W. Yeh, S.K. Chen, S.J. Lin, J.Y. Gan, T.S. Chin, T.T. Shun, C.H. Tsau, S.Y. Chang, Nanostructured high-entropy alloys with multiple principal elements: Novel alloy design concepts and outcomes, Adv. Eng. Mater. 6 (2004) 299-303+274. https://doi.org/10.1002/adem.200300567.

[7] Y. Zhang, T.T. Zuo, Z. Tang, M.C. Gao, K.A. Dahmen, P.K. Liaw, Z.P. Lu, Microstructures and properties of high-entropy alloys, Prog. Mater. Sci. 61 (2014) 1–93. https://doi.org/10.1016/j.pmatsci.2013.10.001.

[8] D.B. Miracle, O.N. Senkov, A critical review of high entropy alloys and related concepts, Acta Mater. 122 (2017) 448–511. https://doi.org/10.1016/j.actamat.2016.08.081.

[9] B. Cantor, I.T.H. Chang, P. Knight, A.J.B. Vincent, Microstructural development in equiatomic multicomponent alloys, Mater. Sci. Eng. A. 375–377 (2004) 213–218. https://doi.org/10.1016/j.msea.2003.10.257.

[10] Z. Li, K.G. Pradeep, Y. Deng, D. Raabe, C.C. Tasan, Metastable high-entropy dual-phase alloys overcome the strength–ductility trade-off, Nature. 534 (2016) 227–230. https://doi.org/10.1038/nature17981.

[11] P. Sarker, T. Harrington, C. Toher, C. Oses, M. Samiee, J.P. Maria, D.W. Brenner, K.S. Vecchio, S. Curtarolo, High-entropy high-hardness metal carbides discovered by entropy descriptors, Nat. Commun. 9 (2018) 1–10. https://doi.org/10.1038/s41467-018-07160-7.

[12] A. Sarkar, L. Velasco, D. Wang, Q. Wang, G. Talasila, L. de Biasi, C. Kübel, T. Brezesinski, S.S. Bhattacharya, H. Hahn, B. Breitung, High entropy oxides for reversible energy storage, Nat. Commun. 9 (2018). https://doi.org/10.1038/s41467-018-05774-5.

[13] M. Gao, D. Alman, Searching for Next Single-Phase High-Entropy Alloy Compositions, Entropy. 15 (2013) 4504–4519. https://doi.org/10.3390/e15104504.

[14] D.J.M. King, S.C. Middleburgh, A.G. McGregor, M.B. Cortie, Predicting the formation and stability of single phase high-entropy alloys, Acta Mater. 104 (2016) 172–179. https://doi.org/10.1016/j.actamat.2015.11.040.

[15] M. Feuerbacher, M. Heidelmann, C. Thomas, Hexagonal High-entropy Alloys, Mater. Res. Lett. 3 (2014) 1–6. https://doi.org/10.1080/21663831.2014.951493.

[16] K.R. Lim, K.S. Lee, J.S. Lee, J.Y. Kim, H.J. Chang, Y.S. Na, Dual-phase high-entropy alloys for high-temperature structural applications, J. Alloys Compd. 728 (2017) 1235–1238. https://doi.org/10.1016/j.jallcom.2017.09.089.

[17] S.T. Chen, W.Y. Tang, Y.F. Kuo, S.Y. Chen, C.H. Tsau, T.T. Shun, J.W. Yeh, Microstructure and properties of age-hardenable AlxCrFe1.5MnNi0.5 alloys, Mater. Sci. Eng. A. 527 (2010) 5818–5825. https://doi.org/10.1016/j.msea.2010.05.052.

[18] T.K. Tsao, A.C. Yeh, C.M. Kuo, K. Kakehi, H. Murakami, J.W. Yeh, S.R. Jian, The High Temperature Tensile and Creep Behaviors of High Entropy Superalloy, Sci. Rep. 7 (2017) 1–9. https://doi.org/10.1038/s41598-017-13026-7.

[19] Y.T. Chen, Y.J. Chang, H. Murakami, T. Sasaki, K. Hono, C.W. Li, K. Kakehi, J.W. Yeh, A.C. Yeh, Hierarchical microstructure strengthening in a single crystal high entropy superalloy, Sci. Rep. 10 (2020) 1–11. https://doi.org/10.1038/s41598-020-69257-8.

[20] A. Munitz, L. Meshi, M.J. Kaufman, Heat treatments' effects on the microstructure and mechanical properties of an equiatomic Al-Cr-Fe-Mn-Ni high entropy alloy, Mater. Sci. Eng. A. 689 (2017) 384–394. https://doi.org/10.1016/j.msea.2017.02.072.

[21] W.R. Wang, W.L. Wang, J.W. Yeh, Phases, microstructure and mechanical properties of AlxCoCrFeNi high-entropy alloys at elevated temperatures, J. Alloys Compd. 589 (2014) 143–152. https://doi.org/10.1016/j.jallcom.2013.11.084.

[22] S. Mohanty, T.N. Maity, S. Mukhopadhyay, S. Sarkar, N.P. Gurao, S. Bhowmick, K. Biswas, Powder metallurgical processing of equiatomic AlCoCrFeNi high entropy alloy: Microstructure and mechanical properties, Mater. Sci. Eng. A. 679 (2017) 299–313. https://doi.org/10.1016/j.msea.2016.09.062.

[23] P. Shi, W. Ren, T. Zheng, Z. Ren, X. Hou, J. Peng, P. Hu, Y. Gao, Y. Zhong, P.K. Liaw, Enhanced strength–ductility synergy in ultrafine-grained eutectic high-entropy alloys by inheriting microstructural lamellae, Nat. Commun. 10 (2019) 1–8. https://doi.org/10.1038/s41467-019-08460-2.

[24] A. Munitz, S. Salhov, S. Hayun, N. Frage, Heat treatment impacts the micro-structure and mechanical properties of AlCoCrFeNi high entropy alloy, J. Alloys Compd. 683 (2016) 221–230. https://doi.org/10.1016/j.jallcom.2016.05.034.

[25] T. Yang, S. Xia, S. Liu, C. Wang, S. Liu, Y. Zhang, J. Xue, S. Yan, Y. Wang, Effects of AL addition on microstructure and mechanical properties of AlxCoCrFeNi High-entropy alloy, Mater. Sci. Eng. A. 648 (2015) 15–22. https://doi.org/10.1016/j.msea.2015.09.034.

[26] T.M. Butler, J.P. Alfano, R.L. Martens, M.L. Weaver, High-Temperature Oxidation Behavior of Al-Co-Cr-Ni-(Fe or Si) Multicomponent High-Entropy Alloys, Jom. 67 (2015) 246–259. https://doi.org/10.1007/s11837-014-1185-7.

[27] J. Lu, Y. Chen, H. Zhang, L. He, R. Mu, Z. Shen, X. Zhao, F. Guo, Y/Hf-doped Al0.7CoCrFeNi high-entropy alloy with ultra oxidation and spallation resistance at 1200 °C, Corros. Sci. 174 (2020) 108803. https://doi.org/10.1016/j.corsci.2020.108803.

[28] A. Mohanty, J.K. Sampreeth, O. Bembalge, J.Y. Hascoet, S. Marya, R.J. Immanuel, S.K. Panigrahi,

High temperature oxidation study of direct laser deposited AlXCoCrFeNi (X=0.3,0.7) high entropy alloys, Surf. Coatings Technol. 380 (2019) 125028. https://doi.org/10.1016/j.surfcoat.2019.125028.

[29] G.R. Holcomb, J. Tylczak, C. Carney, Oxidation of CoCrFeMnNi High Entropy Alloys, Jom. 67 (2015) 2326–2339. https://doi.org/10.1007/s11837-015-1517-2.

[30] Y. Wang, M. Zhang, J. Jin, P. Gong, X. Wang, Oxidation behavior of CoCrFeMnNi high entropy alloy after plastic deformation, Corros. Sci. 163 (2020) 108285. https://doi.org/10.1016/j.corsci.2019.108285.

[31] O.N. Senkov, S. V. Senkova, D.M. Dimiduk, C. Woodward, D.B. Miracle, Oxidation behavior of a refractory NbCrMo 0.5Ta0.5TiZr alloy, J. Mater. Sci. 47 (2012) 6522–6534. https://doi.org/10.1007/s10853-012-6582-0.

[32] T.M. Butler, M.L. Weaver, Oxidation behavior of arc melted AlCoCrFeNi multi-component high-entropy alloys, J. Alloys Compd. 674 (2016) 229–244. https://doi.org/10.1016/j.jallcom.2016.02.257.

[33] J. Lu, Y. Chen, H. Zhang, N. Ni, L. Li, L. He, R. Mu, X. Zhao, F. Guo, Y/Hf-doped AlCoCrFeNi high-entropy alloy with ultra oxidation and spallation resistance, Corros. Sci. 166 (2020) 108426. https://doi.org/10.1016/j.corsci.2019.108426.

[34] J. Lu, H. Zhang, Y. Chen, L. Li, X. Liu, W. Xiao, N. Ni, X. Zhao, F. Guo, P. Xiao, Y-doped AlCoCrFeNi2.1 eutectic high-entropy alloy with excellent oxidation resistance and structure stability at 1000°C and 1100°C, Corros. Sci. 180 (2021). https://doi.org/10.1016/j.corsci.2020.109191.

[35] S.J. Zinkle, K.A. Terrani, J.C. Gehin, L.J. Ott, L.L. Snead, Accident tolerant fuels for LWRs: A perspective, J. Nucl. Mater. 448 (2014) 374–379. https://doi.org/10.1016/j.jnucmat.2013.12.005.

[36] A. Marshal, K.G. Pradeep, D. Music, L. Wang, O. Petracic, J.M. Schneider, Combinatorial evaluation of phase formation and magnetic properties of FeMnCoCrAl high entropy alloy thin film library, Sci. Rep. 9 (2019) 7864. https://doi.org/10.1038/s41598-019-44351-8.

[37] J. Chen, P. Niu, Y. Liu, Y. Lu, X. Wang, Y. Peng, J. Liu, Effect of Zr content on microstructure and mechanical properties of AlCoCrFeNi high entropy alloy, Mater. Des. 94 (2016) 39–44. https://doi.org/10.1016/j.matdes.2016.01.033.

[38] C. Tang, A. Jianu, M. Steinbrueck, M. Grosse, A. Weisenburger, H.J. Seifert, Influence of composition and heating schedules on compatibility of FeCrAl alloys with high-temperature steam, J. Nucl. Mater. 511 (2018) 496–507. https://doi.org/10.1016/j.jnucmat.2018.09.026.

[39] K.A. Unocic, Y. Yamamoto, B.A. Pint, Effect of Al and Cr Content on Air and Steam Oxidation of FeCrAl Alloys and Commercial APMT Alloy, Oxid. Met. 87 (2017) 431–441. https://doi.org/10.1007/s11085-017-9745-1.

[40] A.S. Khanna, Introduction to High Temperature Oxidation and Corrosion, ASM International, 2002.

[41] D. Naumenko, B.A. Pint, W.J. Quadakkers, Current Thoughts on Reactive Element Effects in Alumina-Forming Systems: In Memory of John, Oxid. Met. 86 (2016) 1–43. https://doi.org/10.1007/s11085-016-9625-0.

[42] C. Wang, M. Zinkevich, F. Aldinger, On the thermodynamic modeling of the Zr-O system, Calphad Comput. Coupling Phase Diagrams Thermochem. 28 (2004) 281–292. https://doi.org/10.1016/j.calphad.2004.09.002.

[43] U. Brossmann, R. Würschum, U. Södervall, H.E. Schaefer, Oxygen diffusion in ultrafine grained monoclinic ZrO2, J. Appl. Phys. 85 (1999) 7646–7654. https://doi.org/10.1063/1.370567.

[44] R. DeHoff, Thermodynamics in materials science, CRC Press, 2006.

[45] K.S. Nanjundaswamy, M.N. Sankarshanamurthy, Low-temperature stabilization of pure MnO, Bull. Mater. Sci. 7 (1985) 459–463. https://doi.org/10.1007/BF02744055.

[46] K.Y. Tsai, M.H. Tsai, J.W. Yeh, Sluggish diffusion in Co-Cr-Fe-Mn-Ni high-entropy alloys, Acta Mater. 61 (2013) 4887–4897. https://doi.org/10.1016/j.actamat.2013.04.058.

[47] Y. V. Golikov, S.A. Petrova, A. V. Antonov, V.F. Balakirev, Phase diagrams of the Mn-Al-O system, J. Phys. Chem. Solids. 56 (1995) 767–775. https://doi.org/10.1016/0022-3697(94)00191-X.

[48] S. Chatterjee, I.H. Jung, Critical evaluation and thermodynamic modeling of the Al-Mn-O (Al2O3-MnO-Mn2O3) system, J. Eur. Ceram. Soc. 34 (2014) 1611–1621. https://doi.org/10.1016/j.jeurceramsoc.2013.12.017.

[49] Z.G. Zhang, F. Gesmundo, P.Y. Hou, Y. Niu, Criteria for the formation of protective Al2O3 scales on Fe-Al and Fe-Cr-Al alloys, Corros. Sci. 48 (2006) 741–765. https://doi.org/10.1016/j.corsci.2005.01.012.

[50] S. Yoneda, S. Hayashi, I. Saeki, S. Ukai, Investigation of Initial Transient Oxidation of Fe–xCr– 6at.%Al Alloys Using Synchrotron Radiation During Heating to 1000 °C in Air, Oxid. Met. 86 (2016) 357–370. https://doi.org/10.1007/s11085-016-9641-0.

[51] F.H. Stott, G.C. Wood, J. Stringer, The influence of alloying elements on the development and maintenance of protective scales, Oxid. Met. 44 (1995) 113–145. https://doi.org/10.1007/BF01046725.

[52] J. Engkvist, U. Bexell, M. Grehk, M. Olsson, High temperature oxidation of FeCrAl-alloys - Influence of Al-concentration on oxide layer characteristics, Mater. Corros. 60 (2009) 876–881. https://doi.org/10.1002/maco.200805186.

[53] S.R.J. Saunders, M. Monteiro, F. Rizzo, The oxidation behaviour of metals and alloys at high temperatures in atmospheres containing water vapour: A review, Prog. Mater. Sci. 53 (2008) 775–837. https://doi.org/10.1016/j.pmatsci.2007.11.001.

[54] V. Babic, C. Geers, I. Panas, Reactive Element Effects in High-Temperature Alloys Disentangled, Oxid. Met. (2019). https://doi.org/10.1007/s11085-019-09946-6.

[55] B.A. Pint, Optimization of Reactive-Element Additions to Improve Oxidation Performance of Alumina-Forming Alloys, J. Am. Ceram. Soc. 86 (2003) 686–95. https://doi.org/10.1111/j.1151-2916.2003.tb03358.x.

[56] P. Huczkowski, S.G. Gopalakrishnan, W. Nowak, H. Hattendorf, R. Iskandar, J. Mayer, W.J. Quadakkers, Effect of Zr content on the morphology and emissivity of surface oxide scales on FeCrAlY alloys, Adv. Eng. Mater. 18 (2016) 711–720. https://doi.org/10.1002/adem.201500439.

[57] P. Liang, N. Dupin, S.G. Fries, H.J. Seifert, I. Ansara, H.L. Lukas, F. Aldinger, Thermodynamic assessment of the Zr-O binary system, Zeitschrift Fur Met. 92 (2001) 747–756.

[58] V. Swamy, H.J. Seifert, F. Aldinger, Thermodynamic properties of Y2O3 phases and the yttrium-oxygen phase diagram, J. Alloys Compd. 269 (1998) 201–207. https://doi.org/10.1016/S0925-8388(98)00245-X.

[59] T. Maeda, S. Ukai, S. Hayashi, N. Oono, Y. Shizukawa, K. Sakamoto, Effects of zirconium and oxygen on the oxidation of FeCrAl-ODS alloys under air and steam conditions up to 1500 °C, J. Nucl. Mater. 516 (2019) 317–326. https://doi.org/10.1016/j.jnucmat.2019.01.041.

[60] M. Steinbrück, High-temperature reaction of oxygen-stabilized α-Zr(O) with nitrogen, J. Nucl. Mater. 447 (2014) 46–55. https://doi.org/10.1016/j.jnucmat.2013.12.024.

[61] F. a Golightly, G.C. Wood, F.H. Stott, The Early Stages of Development of Alfa- Alumina Scales on Fe-Cr-Al and Fe-Cr-Al-Y Alloys at High Temperature, Oxid. Met. 14 (1980) 217–234.

[62] H. Götlind, F. Liu, J.-E. Svensson, M. Halvarsson, L.-G. Johansson, The effect of water vapor on the initial stages of oxidation of the FeCrAl alloy Kanthal AF at 900°C, Oxid. Met. 67 (2007) 251–266. https://doi.org/10.1007/s11085-007-9055-0.

[63] J.L. Smialek, Kinetic Aspects of Ti2AlC MAX Phase Oxidation, Oxid. Met. 83 (2015) 351–366. https://doi.org/10.1007/s11085-015-9526-7.

[64] P.J. Meschter, E.J. Opila, N.S. Jacobson, Water Vapor–Mediated Volatilization of High-Temperature Materials, Annu. Rev. Mater. Res. 43 (2013) 559–588. https://doi.org/10.1146/annurev-matsci-071312-121636.

[65] B.A. Pint, K.A. Unocic, K.A. Terrani, Effect of steam on high temperature oxidation behaviour of alumina-forming alloys, Mater. High Temp. 32 (2015) 28–35. https://doi.org/10.1179/0960340914Z.00000000058.

[66] H. Shi, C. Tang, A. Jianu, R. Fetzer, A. Weisenburger, M. Steinbrueck, M. Grosse, R. Stieglitz, G. Müller, Oxidation behavior and microstructure evolution of alumina-forming austenitic & high entropy alloys in steam environment at 1200 °C, Corros. Sci. 170 (2020) 108654. https://doi.org/10.1016/j.corsci.2020.108654.

[67] B.A. Pint, K.A. Terrani, Y. Yamamoto, L.L. Snead, Material Selection for Accident Tolerant Fuel Cladding, Metall. Mater. Trans. E. 2 (2015) 190–196. https://doi.org/10.1007/s40553-015-0056-7.

[68] N.A.P.K. Kumar, C. Li, K.J. Leonard, H. Bei, S.J. Zinkle, Microstructural stability and mechanical behavior of FeNiMnCr high entropy alloy under ion irradiation, Acta Mater. 113 (2016) 230–244. https://doi.org/10.1016/j.actamat.2016.05.007.